Journal of the American College of Cardiology
© 2007 by the American College of Cardiology Foundation
Published by Elsevier Inc.

Vol. 50, No. 18, 2007
ISSN 0735-1097/07/$32.00

CORRESPONDENCE

Research Correspondence

Anti-KCNH2 Antibody-Induced Long QT Syndrome

Novel Acquired Form of Long QT Syndrome

To the Editor: The acquired form of long QT syndrome (LQTS) is often induced by hypokalemia or drugs. Hypokalemia and drugs cause QT prolongation via reduction in the rapidly activating component of the delayed rectifier K^+ currents (I_{Kr}). Therefore, the KCNH2 (HERG) channel conducting I_{Kr} is recognized as the most susceptible channel in acquired LQTS. However, the autoimmune effect on the KCNH2 channel has not been elucidated.

In the present report, we describe a female patient with an acquired form of LQTS with no known cause of QT prolongation. We used the patch clamp method (1) to determine whether her serum and immunoglobulin (Ig)G reduced I_{Kr}, and we performed Western blot analysis to determine whether her IgG included anti-KCNH2 antibodies.

The patient was a 42-year-old female who had a normal clinical history until recurrent episodes of syncope for 3 months. An electrocardiogram (ECG) showed marked QT prolongation, T-wave alternans, and episodes of Torsades de pointes (Fig. 1A). Treatment with atrial pacing (70/min) and intravenous magnesium infusion were started, but the corrected QT interval (QTc) was persistently prolonged (0.70 $s^{0.5}$) (Fig. 1B). The ECGs obtained at annual checkups for the previous 4 years were normal or at most borderline (0.45 to 0.46 for women), but with normal T-wave morphology and not suggestive of LQTS (QTc 0.43 $s^{0.5}$) (Fig. 1C), and there was no family history of QT prolongation or cardiac sudden death. The patient was not taking any drugs, and there was no evidence of structural heart disease or cerebrovascular disease. Laboratory data, including serum electrolytes and hormones, were normal except for detection of increased IgG concentration (1,783 mg/dl) and positive anti-Sjögren's syndrome A (SSA)/Ro antibodies (141.3 index). The recurrence of syncope was diminished by oral administration of atenolol (100 mg/day) and verapamil (120 mg/day). The patient was discharged after implantation of an implantable cardioverter-defibrillator with pacing mode DDI (lower: 70/min). Prolonged QT interval and increased IgG level have remained, but ventricular tachycardia or fibrillation events have not been detected.

We screened for known LQTS-associated genes by polymerase chain reaction DNA conformation polymorphism analysis and DNA sequencing. We suspected LQT2 because of low-amplitude T waves in the ECG, but there was no mutation in the *KCNH2* gene. Furthermore, no mutation was detected in *KCNQ1*, *SCN5A*, *KCNE1*, *KCNE2*, and *KCNJ2* genes. There was a polymorphism (D85N) in *KCNE1*, which is heterozygously found in 2% of the Japanese population. Because ECGs for the previous 4 years were normal, D85N-*KCNE1* may have not a causative but rather a modifying role in this LQTS patient.

The KCNH2 current stably expressed in HEK 293 cells was significantly reduced when cells had been cultured for 1 to 5 days in a medium to which 2% serum from the patient (Figs. 2A and 2D) or IgG (75 μg/ml) (Figs. 2B to 2D) had been added. When cells expressing KCNH2 that had been cultured in the patient's serum were returned to the medium without serum overnight, the amplitudes of both KCNH2 outward and tail currents recovered to untreated levels. The patient's serum had no effect on the slowly activating components of the delayed rectifier K^+ currents (I_{Ks}) of HEK 293 cells expressing KCNQ1/KCNE1 (data not shown). Next, we tested whether the patient's serum has an acute effect on KCNH2 currents (I). Direct application of 2% serum from the patient to physiologic solution for 5 min had no effect on either I_{step} or I_{tail}. These findings suggest that the patient's IgG decreased KCNH2 expression. The mechanism is not clear, but endocytosis may be facilitated.

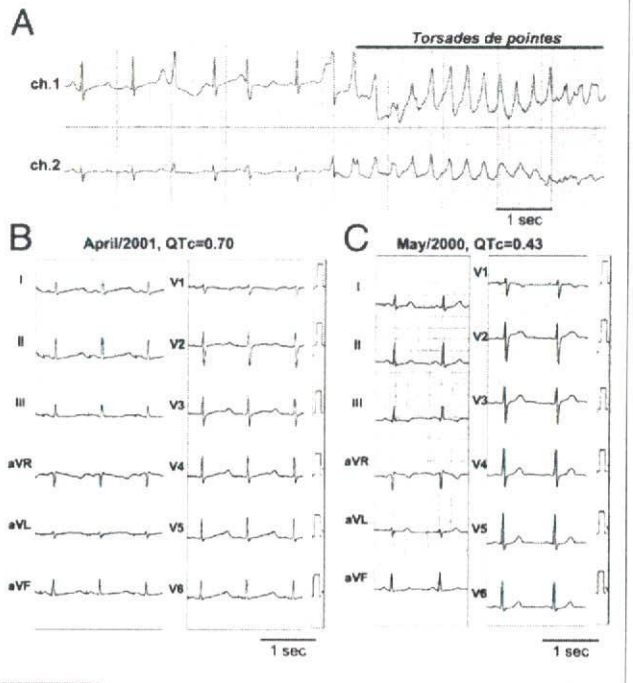

Figure 1 **Electrocardiogram Traces of a Patient With Acquired QT Prolongation**

(A) Marked QT prolongation and Torsades de pointes shown in 24-h electrocardiogram traces. **(B)** Prolonged QT interval was persistently observed after the initial episodes (corrected QT interval [QTc] 0.70 $s^{0.5}$). **(C)** Twelve-lead electrocardiogram 1 year before is normal (QTc 0.43 $s^{0.5}$).

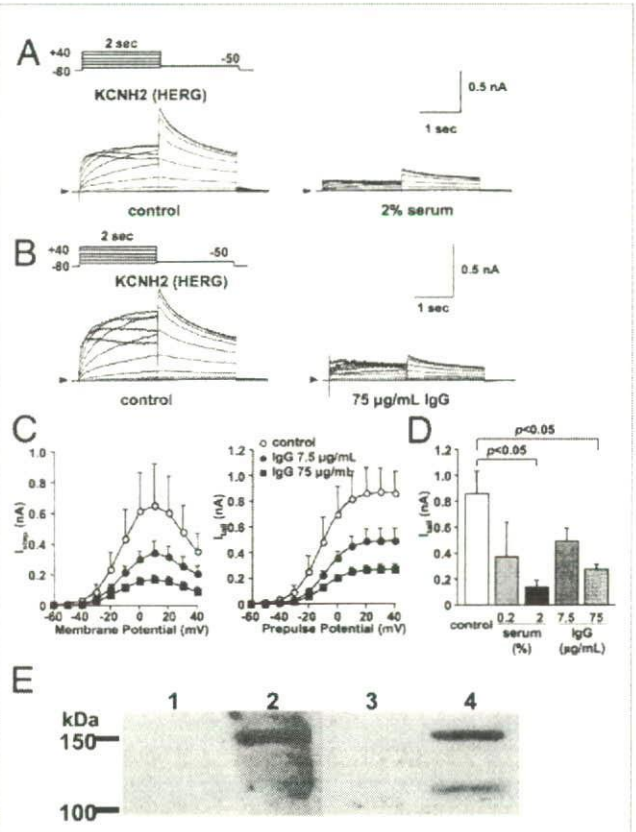

Figure 2 **KCNH2 (HERG) Channel Currents and Western Blot Analysis of Autoantibodies Produced Against KCNH2**

(A) Representative KCNH2 (HERG) channel currents recorded from HEK 293 cells cultured in control medium **(left)** and medium supplemented with 2% serum from the patient **(right)**. **(B)** Representative KCNH2 channel currents recorded from HEK 293 cells cultured in control medium **(left)** and medium supplemented with 75 μg/ml immunoglobulin (Ig)G from the patient **(right)**. **(C)** Current (I)–voltage relationships of I_{step} **(left)** and I_{tail} **(right)** recorded from HEK 293 cells cultured in control medium (**open circles**; n = 4) or a medium supplemented with either 7.5 μg/ml (**solid circles**; n = 7) or 75 μg/ml (**solid squares**; n = 7) IgG. The lines fitted to I_{tail} data **(right)** represent Boltzmann functions. **(D)** A comparison of the dose-dependent effects of serum (0.2% and 2%) and IgG (7.5 and 75 μg/ml) added to the culture medium (control) of HEK 293 cells expressing KCNH2 on maximal I_{tail} amplitude. **(E)** Western blot analysis of autoantibodies produced against KCNH2. **Lane 1**: IgG from a healthy control subject; **lane 2**: IgG from the patient; **lane 3**: pre-incubation of the HEK 293 lysate expressing KCNH2 protein with IgG from the patient; **lane 4**: anti-KCNH2 polyclonal antibodies (positive control).

In Western blotting of the lysate of HEK 293 cells expressing KCNH2, no band was detected in the presence of IgG from a healthy control subject (Fig. 2E, lane 1). A single distinct band of approximately 150 kDa was evident in the presence of IgG from the patient (Fig. 2E, lane 2). This band was absorbed by preincubation with the lysate of HEK 293 cells expressing KCNH2 protein (Fig. 2E, lane 3). A band of the same size was recognized in the presence of rabbit antiHERG polyclonal antibodies (Alomone Labs, Jerusalem, Israel) (Fig. 2E, lane 4). A 155-kDa (upper) band is a mature form of the KCNH2 channel and a 135-kDa (lower) band is a precursor form of the KCNH2 channel (2). Figure 2B shows the upper band in the presence of the patient's IgG. Therefore, the patient's IgG contains autoantibodies against the mature form of KCNH2 protein.

Cross-reaction of anti-SSA/Ro antibodies with the L-type calcium channel has been reported (3). Lazzerini et al. (4) have also reported that patients with anti-SSA/Ro–positive connective tissue diseases show a high prevalence of QTc prolongation. In the present study, the patient had positive anti-SSA/Ro antibodies. Cross-reaction of anti-SSA/Ro antibodies with the KCNH2 channel may be involved in the pathogenesis of autoimmunity. Immunosuppressive therapy and reduction of plasma IgG may be effective for QT-interval shortening in the future. Further studies are needed to clarify this point.

In summary, our results show that abnormal IgG from a patient with acquired LQTS reduces the KCNH2 current and that the IgG includes anti-KCNH2 antibody. This is the first report of anti-KCNH2 antibody-induced LQTS.

***Kazufumi Nakamura, MD, PhD**

*Department of Cardiovascular Medicine
Okayama University Graduate School of Medicine, Dentistry, and Pharmaceutical Sciences
2-5-1 Shikata-cho
Okayama 700-8558
Japan
E-mail: ichibun@cc.okayama-u.ac.jp

Yusuke Katayama, MD, PhD
Kengo F. Kusano, MD, PhD
Kayo Haraoka, MD
Yoshinori Tani, MD
Satoshi Nagase, MD, PhD
Hiroshi Morita, MD, PhD
Daiji Miura, PhD
Yoshihisa Fujimoto, MD, PhD
Tetsushi Furukawa, MD, PhD
Kazuo Ueda, MD
Yoshiyasu Aizawa, MD
Akinori Kimura, MD, PhD
Yoshihisa Kurachi, MD, PhD
Tohru Ohe, MD, PhD, FACC

doi:10.1016/j.jacc.2007.07.037

Please note: Drs. Nakamura and Katayama contributed equally to this work.

REFERENCES

1. Katayama Y, Fujita A, Ohe T, Findlay I, Kurachi Y. Inhibitory effects of vesnarinone on cloned cardiac delayed rectifier K(+) channels expressed in a mammalian cell line. J Pharmacol Exp Ther 2000;294:339–46.
2. Zhou Z, Gong Q, Epstein ML, January CT. HERG channel dysfunction in human long QT syndrome. Intracellular transport and functional defects. J Biol Chem 1998;273:21061–6.
3. Xiao GQ, Qu Y, Hu K, Boutjdir M. Down-regulation of L-type calcium channel in pups born to 52 kDa SSA/Ro immunized rabbits. FASEB J 2001;15:1539–45.
4. Lazzerini PE, Acampa M, Guideri F, et al. Prolongation of the corrected QT interval in adult patients with antiRo/SSA-positive connective tissue diseases. Arthritis Rheum 2004;50:1248–52.

Dominant Negative Suppression of Rad Leads to QT Prolongation and Causes Ventricular Arrhythmias via Modulation of L-type Ca^{2+} Channels in the Heart

Hirotaka Yada, Mitsushige Murata, Kouji Shimoda, Shinsuke Yuasa, Haruko Kawaguchi, Masaki Ieda, Takeshi Adachi, Mitsuru Murata, Satoshi Ogawa, Keiichi Fukuda

Abstract—Disorders of L-type Ca^{2+} channels can cause severe cardiac arrhythmias. A subclass of small GTP-binding proteins, the RGK family, regulates L-type Ca^{2+} current ($I_{Ca,L}$) in heterologous expression systems. Among these proteins, Rad (Ras associated with diabetes) is highly expressed in the heart, although its role in the heart remains unknown. Here we show that overexpression of dominant negative mutant Rad (S105N) led to an increase in $I_{Ca,L}$ and action potential prolongation via upregulation of L-type Ca^{2+} channel expression in the plasma membrane of guinea pig ventricular cardiomyocytes. To verify the in vivo physiological role of Rad in the heart, a mouse model of cardiac-specific Rad suppression was created by overexpressing S105N Rad, using the α-myosin heavy chain promoter. Microelectrode studies revealed that action potential duration was significantly prolonged with visible identification of a small plateau phase in S105N Rad transgenic mice, when compared with wild-type littermate mice. Telemetric electrocardiograms on unrestrained mice revealed that S105N Rad transgenic mice had significant QT prolongation and diverse arrhythmias such as sinus node dysfunction, atrioventricular block, and ventricular extrasystoles, whereas no arrhythmias were observed in wild-type mice. Furthermore, administration of epinephrine induced frequent ventricular extrasystoles and ventricular tachycardia in S105N Rad transgenic mice. This study provides novel evidence that the suppression of Rad activity in the heart can induce ventricular tachycardia, suggesting that the Rad-associated signaling pathway may play a role in arrhythmogenesis in diverse cardiac diseases. (***Circ Res.* 2007;101:69-77.**)

Key Words: G protein ■ L-type Ca^{2+} channels ■ arrhythmia

Rad (Ras associated with diabetes) is the prototypic member of the newly emerging RGK family of proteins, a group of Ras-related GTPases that includes Rad, Gem, and Rem.[1] Rad was initially identified by subtraction cloning as an mRNA overexpressed in skeletal muscle in a subset of patients with type 2 diabetes mellitus.[2] Among the RGK proteins, Rad is abundantly expressed in skeletal and cardiac muscle.[2] It interacts with various signal transduction molecules such as Rho kinase, calmodulin, and calmodulin-dependent protein kinase II, leading to inhibition of their downstream signals.[3–5] In epithelial or fibroblastic cells, overexpression of Rad results in stress fiber and focal adhesion disassembly, implicating an involvement in cytoskeletal regulation through the Rho kinase pathway.[3] In vascular smooth muscle cells, focal gene transduction of Rad attenuates neointimal formation after balloon injury by inhibiting smooth muscle proliferation and migration activated through the Rho kinase pathway.[6] Furthermore, overexpression of Rad in skeletal muscle worsens diet-induced insulin resistance and glucose intolerance, which is consistent with the observed upregulation of Rad in diabetic patients.[7] Despite the critical roles of Rad in diverse biological processes, its function in the heart is still unknown.

Recently, RGK proteins were found to suppress voltage-gated L-type Ca^{2+} currents ($I_{Ca,L}$) in heterologous expression systems and insulin-secreting β cells of the pancreas.[8–10] This was shown to occur via an interaction with Ca^{2+} channel β subunits, and the finding suggests that Rad may play an important role in cellular Ca^{2+} homeostasis. Indeed, overexpression of Gem in PC12 cells and MIN6 cells prevents Ca^{2+}-triggered exocytosis via inhibition of L-type Ca^{2+} channels.[11] In the heart, Ca^{2+} is essential for electrical activity and is a direct activator of the myofilaments in contraction. Among the many Ca^{2+} handling proteins, cardiac L-type Ca^{2+} channels play central roles in initiation of excitation–contraction coupling and in cardiac electrophysiological properties. Abnormal function of Rad in the heart might therefore lead to various cardiac disorders such as arrhythmias or contractile dysfunction.

Original received December 9, 2006; revision received April 10, 2007; accepted May 15, 2007.

From the Cardiopulmonary Division (H.Y., S.Y., M.I., S.O.), Department of Laboratory Medicine (Mitsushige M., Mitsuru M.), Animal Laboratory Center (K.S.), Department of Regenerative Medicine and Advanced Cardiac Therapeutics (H.K., K.F.), and Department of Biochemistry and Integrative Medical Biology (T.A.), School of Medicine, Keio University, Tokyo, Japan.

Correspondence to Mitsushige Murata, MD, PhD, Department of Laboratory Medicine, Keio University, 35 Shinanomachi, Shinjuku-ku, Tokyo 160-8582, Japan. E-mail muratam@cpnet.med.keio.ac.jp

Circulation Research is available at http://circres.ahajournals.org DOI: 10.1161/CIRCRESAHA.106.146399

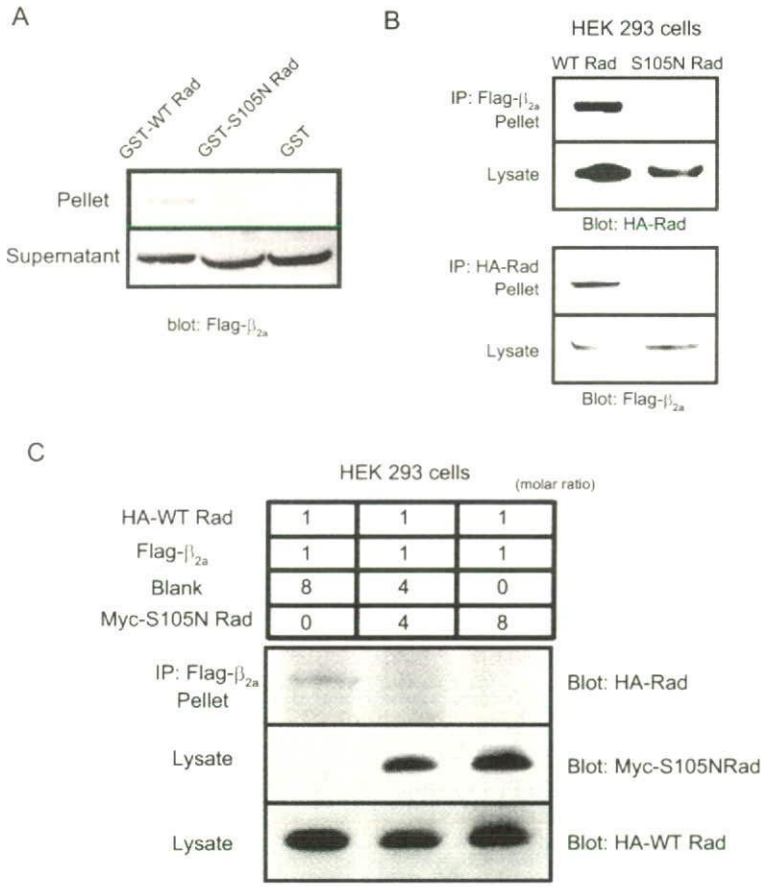

Figure 1. Interaction between Rad and the L-type Ca^{2+} channel β subunit. A, In vitro binding between β_{2a} subunit and WT Rad or S105N Rad. Lysates from Cos7 cells transiently transfected with purified recombinant GST-WT Rad or GST-S105N Rad were incubated with glutathione–Sepharose beads. B, In vivo binding between β_{2a} subunit and WT Rad or S105N Rad. HEK293 cells were cotransfected with hemagglutinin (HA)-tagged Rad and Flag-tagged β_{2a} subunits. The cell lysate was subjected to immunoprecipitation and visualized by immunoblotting with antibodies as indicated. C, Dose-dependent inhibition of the interaction between WT Rad and β subunit by overexpression of S105N Rad. The table denotes the molar ratio of transfected plasmid.

We show here that dominant negative suppression of Rad led to the enhancement of $I_{Ca,L}$ by facilitating channel expression in the plasma membrane of cardiomyocytes, resulting in prolongation of the action potential. Furthermore, transgenic mice with heart-specific overexpression of dominant negative mutant Rad (S105N) displayed ventricular arrhythmias as a consequence of QT prolongation. Our results constitute the first evidence that Rad plays an important role in regulating cardiac electrophysiological properties and that Rad could be a key molecule for understanding the mechanism of arrhythmogenesis in cardiovascular diseases.

Materials and Methods

All experimental procedures and protocols were approved by the Animal Care and Use Committee of Keio University and conformed to the NIH *Guide for the Care and Use of Laboratory Animals*. An expanded Materials and Methods section is available in the online data supplement at http://circres.ahajournals.org.

Myocyte Isolation and Cultures

Myocytes were isolated from the left ventricles of adult guinea pigs and mice using enzymatic digestions as previously described, with slight modifications.[12,13] After isolation, ventricular myocytes were cultured in DMEM containing 10% FBS and 1% penicillin–streptomycin (all from Invitrogen, Carlsbad, Calif) for 24 hours.

Production of S105N Rad Transgenic Mouse

The complete mutant mouse S105N Rad (with the serine at the 105-aa position substituted to arginine, to inhibit GTP binding) cDNA construct was subcloned into the region downstream of the α-myosin heavy chain promoter[14] previously subcloned into the PBS2 SK+ plasmid. The complete transgene was isolated using *Not*I digestion of the PBS2 SK− plasmid. Transgenic mice were generated by the Animal Laboratory Center of Keio University by cDNA microinjection of fertilized C57BL/6×SJL oocytes using standard techniques.

Statistical Analysis

All data are shown as means±SEM. Statistical differences were determined using repeated-measures ANOVA, and $P<0.05$ was considered significant.

Results

Rad Interacts With L-Type Ca^{2+} Channel β Subunits

Previous reports have shown that Rad interacts with Ca^{2+} channel β subunits in heterologous expression systems, resulting in the inhibition of $I_{Ca,L}$.[15,16] To examine whether Rad physically interacts with the β subunits, glutathione *S*-transferase (GST) pull-down assays were performed. As shown in Figure 1A, recombinant GST wild-type (WT) Rad bound to the β subunits in whole-cell extracts derived from transfected Cos7 cells, whereas GST-S105N Rad did not. Furthermore, interaction between Rad and β subunits was confirmed in the context of the cellular environment. HEK293 cells were transiently transfected with Flag-tagged β_{2a} subunits and hemagglutinin-tagged WT Rad or S105N Rad. After 24 hours in culture, coimmunoprecipitation assays were performed. Consistent with the previous report,[15] the β_{2a}

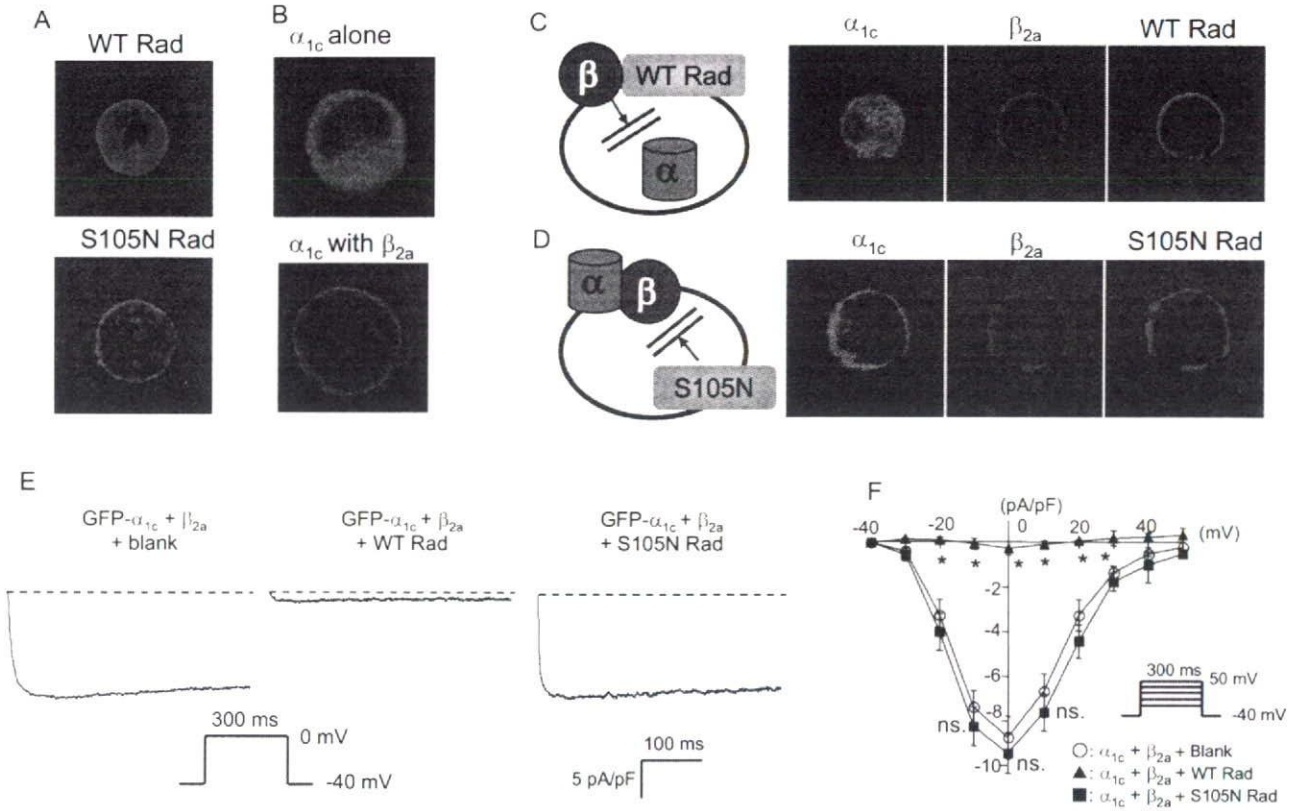

Figure 2. Rad regulates L-type Ca^{2+} channel function via α subunit trafficking to plasma membrane. A, Localization of WT Rad and S105N Rad in HEK293 cells. B, Localization of Ca^{2+} channel α_{1c} subunits in HEK293 cells, when expressed with or without β_{2a} subunit. C and D, Subcellular localization of GFP-α_{1c} subunit (green) and Flag-tagged β_{2a} subunit (blue) in a cell coexpressing hemagglutinin-tagged WT Rad or S105N Rad (red). The localizations of each subunit are depicted diagrammatically on the left. E, Representative Ba^{2+} current traces in HEK293 cells transiently cotransfected with GFP-α_{1c} subunit, β_{2a} subunit, and blank, WT Rad, or S105N Rad. Dashed lines indicate 0 current. F, Current/voltage relationships of Ba^{2+} currents in HEK293 cells cotransfected with GFP-α_{1c} subunit, β_{2a} subunit, and blank (n=7), GFP-α_{1c} subunit, β_{2a} subunit, and WT Rad (n=4), or GFP-α_{1c} subunit, β_{2a} subunit, and S105N Rad (n=6). ns indicates not significant vs control. *$P<0.01$ vs control.

subunits showed an interaction with WT Rad (Figure 1B), but no interaction with S105N Rad was detected. Because S105N Rad, which could bind GDP but not GTP, is known to function as a dominant negative mutant in the regulation of neointimal formation after vascular injury,[6] we examined whether S105N Rad showed dominant negative inhibition of the interaction between WT Rad and β subunits. A plasmid encoding S105N Rad fused with Myc tag at its N terminus was cotransfected with WT Rad and β_{2a}-subunit plasmids into HEK293 cells. As shown in Figure 1C, Myc-tagged S105N Rad suppressed the interaction between WT Rad and β_{2a} subunits in a dose-dependent manner, indicating that S105N Rad did function as a dominant negative mutant for the interaction between WT Rad and β_{2a} subunits.

Based on these results, we next studied whether the interaction between Rad and the β subunit affected the trafficking of Ca^{2+} channel α subunit to the plasma membrane. To do this, green fluorescent protein (GFP)-fused $Ca_v1.2$ (cardiac α_{1c} subunit) and β_{2a} subunit were coimmunostained with WT Rad or S105N Rad in HEK293 cells and visualized by confocal microscopy. Both WT Rad and S105N Rad were localized at the plasma membrane, when expressed alone (Figure 2A). Although individually expressed α_{1c} subunit was localized mainly in the cytoplasm (Figure 2B), cotransfection with β_{2a} subunits resulted in the translocation of α_{1c} subunits from the cytoplasm to plasma membrane, confirming that the β subunit plays a chaperon-like role with the α_{1c} subunit (Figure 2B). When WT Rad was expressed together with both the α_{1c} and β_{2a} subunits, the α_{1c} subunit showed a cytoplasmic distribution, whereas WT Rad and the β_{2a} subunit were still colocalized at the plasma membrane, indicating that WT Rad disrupted the binding of α_{1c} subunit to β_{2a} subunit (Figure 2C). In contrast, S105N Rad did not affect the localization of the α_{1c} and β_{2a} subunits (Figure 2D). These results indicated that the interaction between Rad and the β subunit regulated the trafficking of the α_{1c} subunit to the plasma membrane.

To examine whether Rad regulates the function of L-type Ca^{2+} channels, we recorded Ba^{2+} currents in HEK293 cells using the whole-cell patch clamp technique. Currents conducted by L-type Ca^{2+} channels were recorded with 4 mmol/L Ba^{2+} in the external solution as a charge carrier. The currents in cells in which S105N Rad was coexpressed with GFP-α_{1c} subunit and β_{2a} subunit were similar to those in control cells (average current densities for GFP-α_{1c} subunit, β_{2a} subunit, and S105N Rad: 9.4±0.9 pA/pF [n=6]; for GFP-α_{1c} subunit, β_{2a} subunit, and blank: 8.8±0.9 pA/pF [n=7]; not significant), whereas in cells expressing the GFP-α_{1c} subunit, β_{2a}

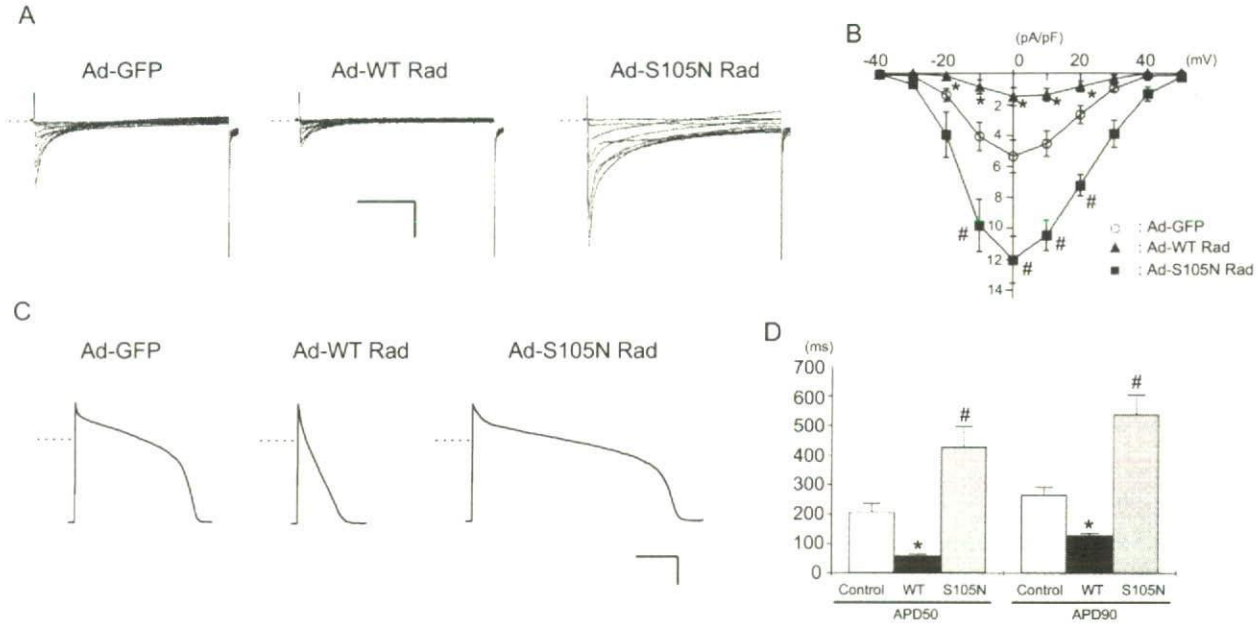

Figure 3. Effects of Rad on L-type Ca^{2+} current and action potential configuration in guinea pig ventricular cardiomyocytes. A, Representative $I_{Ca,L}$ traces in an Ad-GFP–transduced (control) cell, an Ad-WT Rad–transduced cell, and an Ad-S105N Rad–transduced cell. Dashed lines indicate 0 current. B, Current/voltage relationships of $I_{Ca,L}$ in control (n=8), Ad-WT Rad–transduced (n=6), and Ad-S105N Rad–transduced (n=7) cells. #$P<0.05$ vs control, *$P<0.01$ vs control. C, Representative action potential traces in a control cell, an Ad-WT Rad–transduced cell, and an Ad-S105N Rad–transduced cell. Dashed lines indicate 0 mV. D, Pooled data for APD in control (n=8), Ad-WT Rad–transduced (n=5), and Ad-S105N Rad–transduced (n=6) cells. #$P<0.05$ vs control, *$P<0.01$ vs control.

subunit, and WT Rad, the currents were very small (0.20 ± 0.03 pA/pF [n=5] versus control; $P<0.01$), and similar to those in cells expressing GFP-α_{1c} subunit alone (0.19 ± 0.04 pA/pF [n=5]), indicating the association of WT Rad-mediated suppression with the β subunit (Figure 2E and 2F). These results confirmed that WT Rad dramatically suppressed the function of the L-type Ca^{2+} channel, whereas S105N Rad did not.

Rad Regulates $I_{Ca,L}$ via Inhibition of α subunit trafficking to Plasma Membrane in Guinea Pig Ventricular Cardiomyocytes

To investigate the physiological role of Rad in the heart, we transduced adenovirus (Ad) encoding WT Rad or S105N Rad into guinea pig ventricular cardiomyocytes and recorded $I_{Ca,L}$ using the whole-cell patch clamp technique. Interestingly, the peak $I_{Ca,L}$ was larger in the cells overexpressing S105N Rad than in controls (12.0 ± 1.5 pA/pF at 0 mV [n=7] in Ad-S105N Rad–transduced cells versus 5.4 ± 1.0 pA/pF at 0 mV [n=8] in Ad-GFP transduced controls; $P<0.05$), whereas $I_{Ca,L}$ was dramatically smaller in cells overexpressing WT Rad (1.4 ± 0.1 pA/pF at 0 mV [n=6] in Ad-WT Rad–transduced cells versus control; $P<0.01$) (Figure 3A and 3B). Because S105N Rad itself does not affect the $I_{Ca,L}$, as shown in Figure 2F, enhancement of $I_{Ca,L}$ by S105N Rad in cardiomyocytes might be attributable to the dominant negative suppression of endogenous Rad activity. Because the L-type Ca^{2+} channel contributes to the ion influx and plateau phase of the cardiac action potential, we investigated whether Rad-mediated regulation of $I_{Ca,L}$ might affect the action potential in heart cells. Action potentials were recorded in guinea pig ventricular cells transduced with Ad-GFP (control), Ad-WT Rad, and Ad-S105N Rad. As expected, overexpression of WT Rad resulted in a dramatic shortening of the action potential duration (APD) and abolished the robust action potential plateau (APD_{90} 128 ± 7.76 ms [n=5] in Ad-WT Rad–transduced cells versus 267 ± 26.3 ms [n=8] in Ad-GFP–transduced control cells; $P<0.01$), whereas S105N Rad significantly prolonged the APD without changing the action potential configuration (538 ± 70.0 ms [n=6] in Ad-S105N Rad–transduced cells versus control; $P<0.01$) (Figure 3C and 3D).

To investigate the mechanisms of Rad-mediated regulation of $I_{Ca,L}$ in native guinea pig cardiomyocytes, we performed cell fractionation and used Western blot analysis to quantify the expression of α_{1c} subunit in the plasma membrane of cells after 24 hours in culture. The amount of α_{1c} subunit protein extracted from the membrane fraction was significantly lower in Ad-WT Rad–transduced cells than in Ad-GFP–transduced control cells, whereas the overexpression of S105N Rad resulted in a significantly greater extraction of α_{1c} subunit protein from the membrane fraction (Figure 4). These findings show that dominant negative suppression of endogenous Rad by S105N Rad increased Ca^{2+} channel expression at the plasma membrane, thereby implicating endogenous Rad in the regulation of cardiac L-type Ca^{2+} channel expression in the physiological context.

In Vivo Phenotype of Dominant Negative Suppression of Rad in Mouse Heart

To investigate the physiological role of endogenous Rad in vivo, we took advantage of the dominant negative mutant Rad

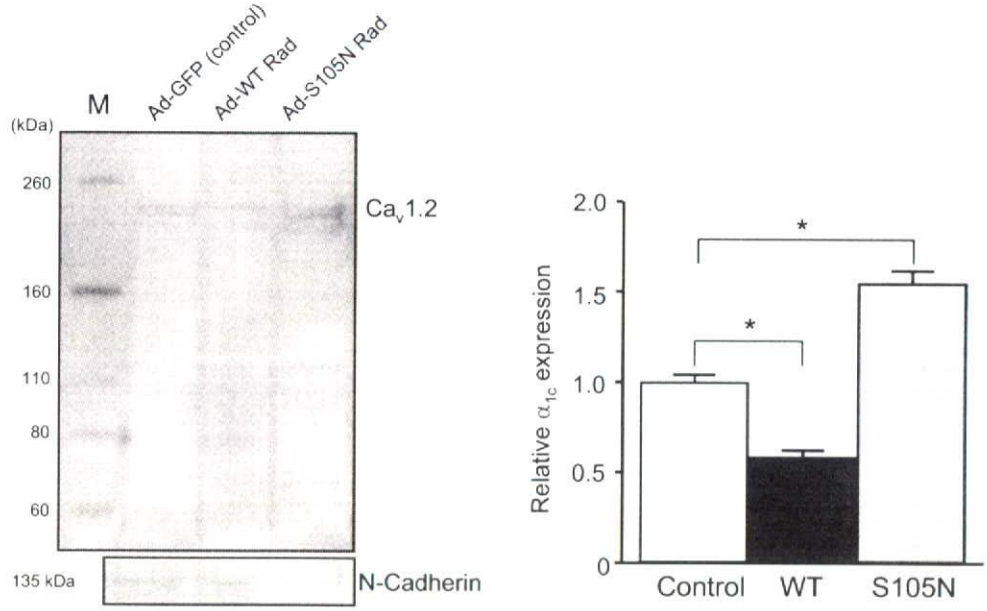

Figure 4. Rad modulates L-type Ca^{2+} channel membrane expression in guinea pig ventricular cardiomyocytes. Quantitative Western blot analysis comparing α_{1c} subunit protein extracted from plasma membranes of cardiomyocytes transduced with Ad-GFP (control), Ad-WT Rad, or Ad-S105N Rad after 24 hours in culture. N-Cadherin was used as an internal control for the membrane protein fraction. M indicates molecular size markers. Data are from 5 independent experiments. *$P<0.05$ vs control.

to engineer an in vivo model of Rad disruption, obtained by overexpressing the S105N Rad under the control of the α-myosin heavy chain promoter. In transgenic (TG) mice aged 12 weeks, the total Rad protein expression in whole heart was 6 times greater than in their WT littermates (Figure 5A), indicating that the expression level of S105N Rad was approximately 5 times that of endogenous Rad. This level of exogenous S105N Rad expression in TG mice should have been sufficient to suppress the endogenous Rad/β subunit interaction, as shown in Figure 1B. Thus, we performed coimmunoprecipitation assays to confirm the effect of S105N Rad overexpression on the endogenous Rad/β subunit interaction in whole hearts. As shown in Figure 5B, the total amount of Rad that bound to the β subunits was much less in S105N TG mouse heart than that in WT mouse heart. Furthermore, we used Western blot analysis to compare α_{1c} protein expression in the plasma membranes of S105N Rad TG and WT mice. The α_{1c} protein expression was significantly greater in S105N Rad TG mice than WT mice, supporting the proposition that dominant negative suppres-

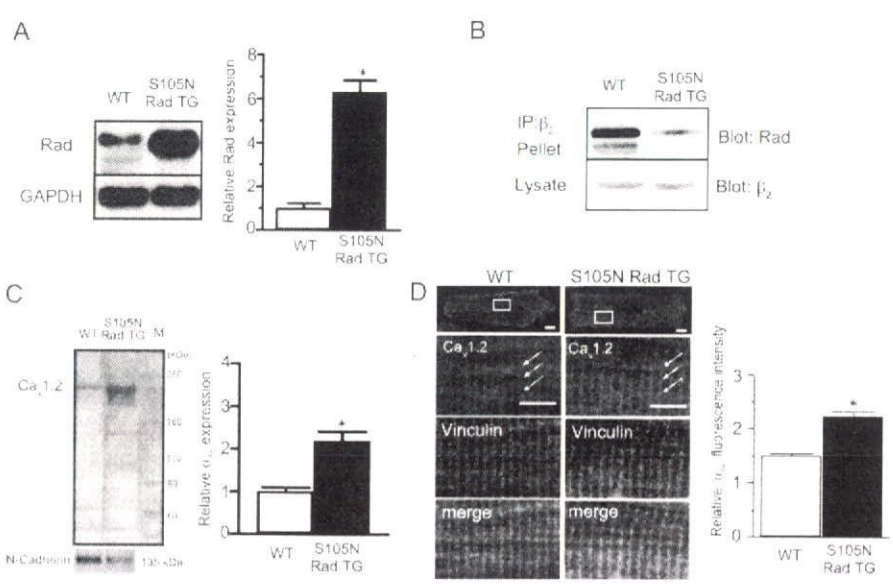

Figure 5. S105N Rad suppresses the in vivo interaction between Rad and β subunit in the heart. A, Western blot analysis comparing total Rad protein level in cardiac muscle from WT and S105N Rad TG mice. Data are from 5 WT and 5 S105N Rad TG mice. *$P<0.05$ vs WT. B, In vivo interaction between Rad and β subunit in the heart. Lysates from whole heart were coimmunoprecipitated with anti-β_2 subunit antibody, and associated Rad proteins were detected by Western blotting. C, Western blot of cardiac α_{1c} subunit protein in the membrane fraction from WT and S105N Rad TG mouse hearts. N-Cadherin was used as an internal control for the membrane fraction. M indicates molecular size markers. Data are from 5 WT and 5 S105N Rad TG mice. *$P<0.05$ vs WT. D, Immunohistochemical analysis of α_{1c} subunits in WT and S105N Rad TG ventricular cardiomyocytes. The white squares in the upper panels indicate the regions shown at higher magnification below. Vinculin was used as a T-tubule marker. Scale bar=10 μm. Pooled data for relative α_{1c} mean fluorescence in WT (n=10) and S105N Rad TG mouse cardiomyocytes (n=10).

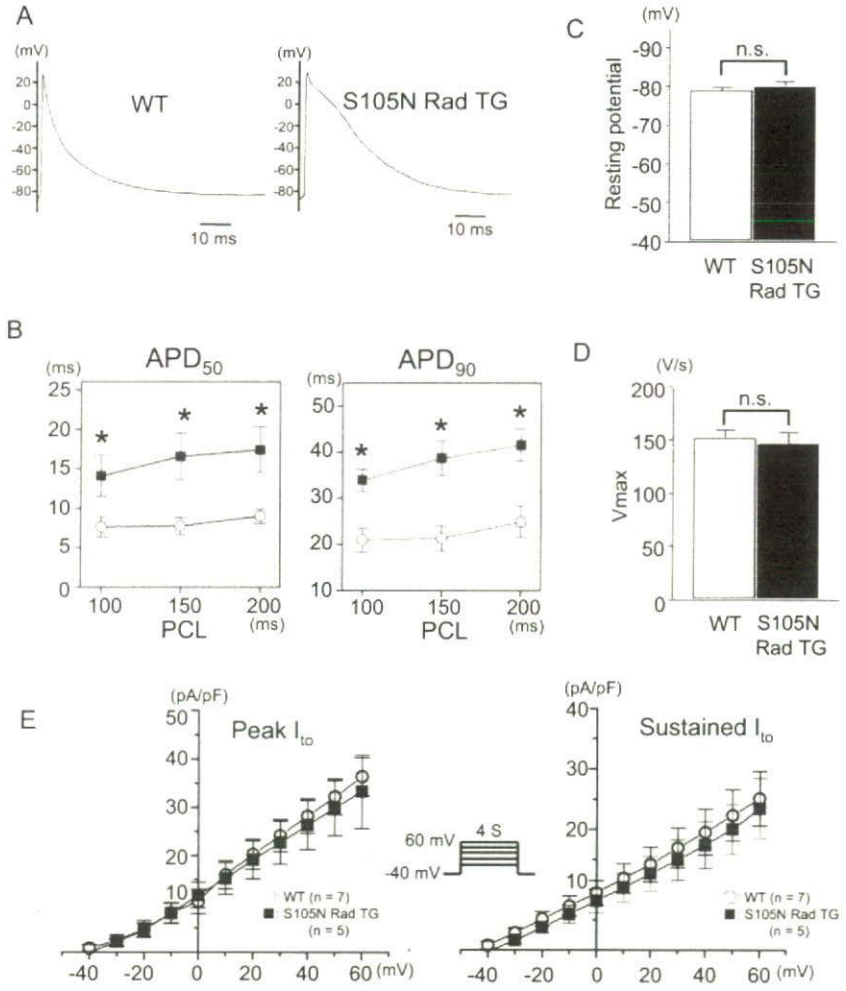

Figure 6. A, Representative action potential traces recorded from papillary muscle samples from WT and S105N Rad TG mice. B, Effects of pacing cycle length (PCL) on APD at 50% (APD_{50}) and 90% (APD_{90}) repolarization in WT (filled circles; n 8) and S105N Rad TG mice (filled squares; n=8). *$P<0.05$ vs WT. C, Pooled data for resting membrane potential recorded from papillary muscles of WT (n=8) and S105N Rad TG mice (n=8). D, Pooled data for V_{max} recorded from papillary muscles of WT (n=8) and S105N Rad TG mice (n=8). E, Current/voltage relationships of I_{to} peak and sustained currents in WT (n=8) and S105N Rad-TG mouse cells (n=5). ns indicates not significant vs WT cells.

sion of Rad facilitates α_{1c} subunit expression at the plasma membrane (Figure 5C). Accordingly, immunohistological analysis revealed that the T tubules of ventricular cardiomyocytes isolated from S105N Rad TG mouse hearts were more intensely immunoreactive for α_{1c} subunits than those of WT mice (Figure 5D). The relative mean fluorescence of α_{1c} subunits in the T-tubule areas to that in non–T-tubule area (between T tubules) were significantly greater in the S105N Rad TG mouse cells than in the WT mouse cells, indicating that S105N Rad facilitated the α_{1c} subunit trafficking to the T tubules in cardiomyocytes (Figure 5D).

Next, action potentials were recorded from left ventricular papillary muscles using conventional microelectrode techniques. The APD was measured at 3 different pacing cycle lengths (100 ms, 150 ms, and 200 ms). As shown in Figure 6A, the APD was prolonged, and a subtle plateau phase was observed in S105N Rad TG mice. Consistent with the in vitro data in guinea pig cells, the APD_{50} and APD_{90} were both longer in S105N Rad TG mice than in WT mice at each pacing cycle length (Figure 6B; APD_{90} at 100 ms pacing cycle length, 33.9±2.5 ms [n=8] in S105N TG mice, versus 20.9±2.6 ms [n=8] in WT mice; $P<0.05$). There were no significant differences in resting membrane potential or V_{max} between WT and TG mice (Figure 6C and 6D), suggesting that dominant negative suppression of Rad did not affect the inward rectifying K^+ currents and Na^+ currents. We also examined the transient outward potassium current (I_{to}), which mainly affects repolarization in the mouse action potential. There were no significant differences between the WT and S105N Rad TG mice in either peak or sustained I_{to} current densities, implying that Rad did not affect I_{to} function (Figure 6E).

As expected from the APD data, surface electrocardiograms showed QT prolongation in S105N Rad TG mice compared with WT mice (Figure 7A). Both QT and QTc intervals in S105N Rad TG mice were significantly longer than those in WT mice (QTc, 60.1±3.0 ms [n=8] in S105N Rad TG mice, versus 47.3±3.3 ms [n=8] in WT mice; $P<0.05$; Figure 7B). No significant differences were detected in other ECG parameters, such as RR, PR, and QRS intervals, as described in Table I in the online data supplement. Given the importance of QT prolongation as a cause of lethal ventricular arrhythmias, we investigated whether the dominant negative suppression of endogenous Rad activity produced arrhythmias in S105N Rad TG mice. In vivo ECGs were recorded from freely moving mice for 24 hours. No arrhythmias were observed in the recordings from WT mice (n=8). In contrast, among the TG mice (n=8), we recorded

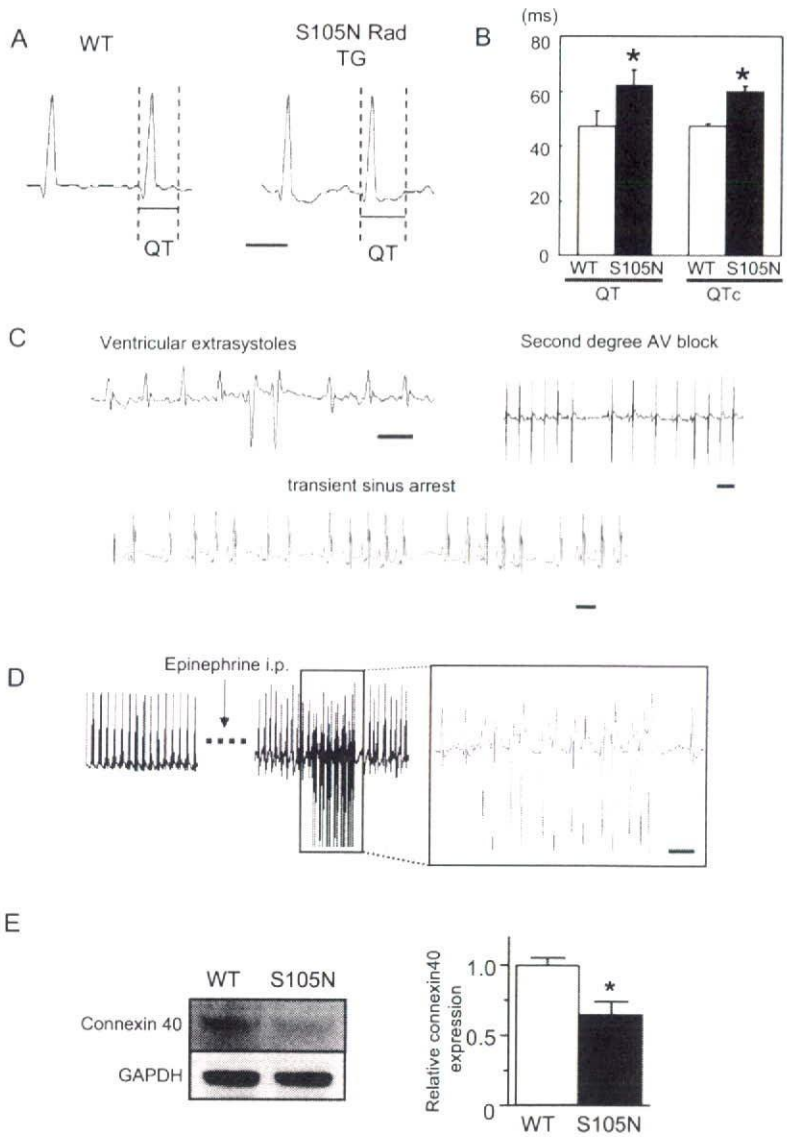

Figure 7. Characteristics of ECGs in S105N Rad TG mice. A, ECG recordings from a WT and a S105N Rad TG mouse. Scale bar=50 ms. B, Pooled data for QT and QTc intervals recorded from WT (n=8) and S105N Rad TG mice (n=8). *$P<0.05$ vs WT. C, Telemetric ECG recording from a freely moving S105N Rad TG mouse. Second degree atrioventricular (AV) block, transient sinus arrest, and frequent ventricular extrasystoles were recorded in S105N Rad TG mice during normal activity. Scale bar=100 ms. D, Nonsustained ventricular tachycardia was induced by intraperitoneal injection of epinephrine in S105N Rad TG mice. Scale bar=100 ms. E, Western blot analysis comparing connexin40 protein level in atrial tissues from WT and S105N Rad TG mice. Data are from 4 WT and 4 S105N Rad TG mice. *$P<0.05$ vs WT.

transient sinus arrest and second-degree atrioventricular block in 6 mice each, and ventricular extrasystoles in 5 mice (Figure 7C). In some patients with long QT syndrome, fatal ventricular arrhythmias occur under physical exertion and emotional stress.[17,18] To mimic these circumstances, we injected epinephrine (2 mg/kg) into the peritoneum of S105N Rad TG mice (n=8) and WT mice (n=8). Under the epinephrine loading, nonsustained ventricular tachycardia was induced in 3 of the TG mice (Figure 7D), and consecutive ventricular extrasystoles were more frequently observed (7 TG mice), although no ventricular arrhythmias were observed in WT mice (see supplemental Table II).

Because the increase in $I_{Ca,L}$ should facilitate nodal conduction, the abnormal nodal function observed in TG mice seemed anomalous. Rad is also known to suppress the Rho signaling pathway by direct interaction with its substrate, ROCK.[5] Furthermore, disruption of Rho signaling results in progressive atrioventricular conduction defects, probably attributable to a dramatic decrease of connexin40.[19,20] We examined the atrial expression of connexin40 in mouse hearts by Western blot analysis. As expected, connexin40 expression was significantly lower in S105N Rad TG mice than WT mice (Figure 7E).

Discussion

The major finding of this study was that dominant negative suppression of endogenous Rad in the heart resulted in an increase in $I_{Ca,L}$, via upregulation of L-type Ca^{2+} channel expression at the plasma membrane. Using a transgenic approach for cardiac-specific inhibition of Rad by expressing the dominant negative form of Rad (S105N), the present study provides important new insights into the physiological function of Rad in regulating cardiac electrophysiology. Although mouse echocardiography showed no significant changes in cardiac size or function in transgenic animals at 12 weeks of age (supplemental Figure I), the phenotype of the transgenic animals comprised a prolonged QT interval, nodal dysfunction, and extrasystoles. These ECG phenotypes were

accompanied by prolonged APDs and enhanced $I_{Ca,L}$, which were attributable to the upregulation of L-type Ca^{2+} channels in T tubules. Under baseline conditions, TG mice displayed ventricular extrasystoles but no ventricular tachycardia. Furthermore, epinephrine administration exacerbated the ventricular arrhythmias in TG mice but did not induce arrhythmias in WT mice. These data indicate that the Rad signaling pathway plays an important role in cardiac antiarrhythmia via the strong suppression of $I_{Ca,L}$.

We did not predict any nodal dysfunction in TG mice because an increase of $I_{Ca,L}$ would be expected to facilitate nodal conduction. The induction of nodal dysfunction was probably attributable, at least in part, to the reduction of connexin40 expression in TG mice. Previous studies have shown that Rad binds directly to ROCK, resulting in the inhibition of Rho/ROCK signaling pathways,[3,6] which regulates the connexin40 expression in mouse hearts.[19] The GST pull-down assays revealed that S105N Rad, as well as WT Rad, could physically interact with ROCK (data not shown). This implies that overexpression of S105N Rad in TG mice may have led to a decrease of connexin40 expression via suppression of the Rho signaling pathways. Furthermore, this inhibitory effect of Rad on Rho pathways was likely to have been especially strong in the heart because Rad binds to ROCK2, which is highly expressed in the heart, whereas the other isoform (ROCK1) is preferentially expressed in noncardiac tissues such as lung, liver, spleen, kidney, and testis.[21] This distinct tissue-specific expression of ROCK isoforms might explain the opposite effects of Gem and Rad on nodal conduction because Gem predominantly binds to ROCK1.[3] However, further studies are needed to test this hypothesis.

One major cause of mortality in patients with diabetes mellitus is diabetic cardiomyopathy, which occurs independently from diabetes-mediated vascular complications. Pereira et al[22] reported that the systolic dysfunction of type 2 diabetic mice is partly attributable to a reduction of $I_{Ca,L}$, implicating Rad-mediated Ca^{2+} channel regulation as a possible factor in diabetic cardiomyopathy. Furthermore, diabetic cardiomyopathy is characterized by electrical remodeling, metabolic remodeling with malignant biochemical processes, and anatomical remodeling with progressive loss of cardiomyocytes.[23] The abnormal prolongation of QT interval is the most prominent electrical remodeling that occurs in diabetic hearts. QT prolongation is a significant predictor of mortality in diabetes patients because it is associated with an increased risk of sudden cardiac death caused by lethal ventricular arrhythmias.[24] One of the mechanisms for QT prolongation in diabetes mellitus is depression of multiple ion currents including the transient outward current, $I_{Ca,L}$, and the delayed rectifier K^+ current.[22,25] Given that Rad mRNA is upregulated in type 2 diabetes patients[2] and Rad protein expression in diabetic mouse heart is upregulated relative to WT mice (data not shown), Rad-mediated regulation of $I_{Ca,L}$ might be involved in the electrophysiological remodeling in diabetic cardiomyopathy. Dominant negative suppression of Rad led to QT prolongation and induction of arrhythmias even in the nondiabetic mice used in this study. Considering these experimental and clinical data, it is plausible that upregulation of Rad in diabetic patients might function as a negative regulator to counteract QT prolongation by compensating for the decreased outward K^+ currents with downregulation of $I_{Ca,L}$. If so, the preservation of Rad function might be a potential strategy for the prevention of lethal ventricular arrhythmias in diabetic cardiomyopathy.

Our data clearly demonstrated that Rad regulated the trafficking of Ca^{2+} channel α subunit in both heterologous systems and cardiomyocytes. However, the precise mechanisms of RGK protein-mediated modulation of L-type Ca^{2+} channels remain to be clarified. Consistent with our data, Beguin et al[9] showed that inhibition of $I_{Ca,L}$ by another RGK protein, Gem, is attributable to the decreased expression of α subunits in the plasma membrane. However, in our study, the complete inhibition of $I_{Ca,L}$ 24 hours after transduction of WT Rad in guinea pig cells could not be explained solely by the suppression of α subunit trafficking to the plasma membrane because our Western blot data still detected a small amount of Ca^{2+} channel expression in the T tubules. These channels may have remained because the turnover of L-type Ca^{2+} channels in the plasma membrane is 36 to 48 hours[26]; thus a 24 hour culture period might not be sufficient for the complete degradation of preexisting channels. Therefore, other mechanisms for suppression of $I_{Ca,L}$ by Rad, unrelated to trafficking, are also likely to be involved. One possibility is the direct inhibition of L-type Ca^{2+} channels by association of Rad with channel subunits. Rem2 has recently been shown to almost completely suppress $I_{Ca,L}$ without altering channel expression at the plasma membrane,[27,28] which supports this hypothesis. The possibility remains that Rad may regulate the expression of other RGK proteins, which in turn alter L-type Ca^{2+} channel function. However, the expression level of Rem protein did not change with overexpression of Rad (data not shown), which leads us to conclude that Rem is not associated with the Rad-mediated regulation of the L-type Ca^{2+} channel. Further studies are required to identify the multiple mechanisms involved in regulation of the L-type Ca^{2+} channel by Rad.

In summary, dominant negative suppression of Rad in the heart induced QT prolongation and ventricular arrhythmias, caused by the augmentation of $I_{Ca,L}$. The finding that Rad regulates L-type Ca^{2+} channel function in the heart suggests that the Rad-associated signaling pathway may play a role in arrhythmogenesis in diverse cardiac diseases.

Acknowledgments

We thank Dr Shunichiro Miyoshi and Dr Yoko Hagiwara for useful technical advice.

Sources of Funding

This study was supported by research grants from the Ministry of Education, Science and Culture, Japan (to M.M., T.A., and K.F.); from Keio Gijuku Academic Developmental Funds (to M.M.); from the Program for Promotion of Fundamental Studies in Health Sciences of the National Institute of Biomedical Innovation (to K.F.); and from health sciences research grants from the Ministry of Health, Labour and Welfare, Japan (H18-Research on Human Genome-002 to S.O.).

Disclosures

None.

References

1. Kelly K. The RGK family: a regulatory tail of small GTP-binding proteins. *Trends Cell Biol.* 2005;15:640–643.
2. Reynet C, Kahn CR. Rad: a member of the Ras family overexpressed in muscle of type II diabetic humans. *Science.* 1993;262:1441–1444.
3. Ward Y, Yap SF, Ravichandran V, Matsumura F, Ito M, Spinelli B, Kelly K. The GTP binding proteins Gem and Rad are negative regulators of the Rho-Rho kinase pathway. *J Cell Biol.* 2002;157:291–302.
4. Moyers JS, Bilan PJ, Zhu J, Kahn CR. Rad and Rad-related GTPases interact with calmodulin and calmodulin-dependent protein kinase II. *J Biol Chem.* 1997;272:11832–11839.
5. Beguin P, Mahalakshmi RN, Nagashima K, Cher DH, Kuwamura N, Yamada Y, Seino Y, Hunziker W. Roles of 14-3-3 and calmodulin binding in subcellular localization and function of the small G-protein Rem2. *Biochem J.* 2005;390:67–75.
6. Fu M, Zhang J, Tseng YH, Cui T, Zhu X, Xiao Y, Mou Y, De Leon H, Chang MM, Hamamori Y, Kahn CR, Chen YE. Rad GTPase attenuates vascular lesion formation by inhibition of vascular smooth muscle cell migration. *Circulation.* 2005;111:1071–1077.
7. Ilany J, Bilan PJ, Kapur S, Caldwell JS, Patti ME, Marette A, Kahn CR. Overexpression of Rad in muscle worsens diet-induced insulin resistance and glucose intolerance and lowers plasma triglyceride level. *Proc Natl Acad Sci U S A.* 2006;103:4481–4486.
8. Finlin BS, Mosley AL, Crump SM, Correll RN, Ozcan S, Satin J, Andres DA. Regulation of L-type Ca^{2+} channel activity and insulin secretion by the Rem2 GTPase. *J Biol Chem.* 2005;280:41864–41871.
9. Beguin P, Nagashima K, Gonoi T, Shibasaki T, Takahashi K, Kashima Y, Ozaki N, Geering K, Iwanaga T, Seino S. Regulation of Ca^{2+} channel expression at the cell surface by the small G-protein kir/Gem. *Nature.* 2001;411:701–706.
10. Murata M, Cingolani E, McDonald AD, Donahue JK, Marban E. Creation of a genetic calcium channel blocker by targeted gem gene transfer in the heart. *Circ Res.* 2004;95:398–405.
11. Sasaki T, Shibasaki T, Beguin P, Nagashima K, Miyazaki M, Seino S. Direct inhibition of the interaction between alpha-interaction domain and beta-interaction domain of voltage-dependent Ca^{2+} channels by Gem. *J Biol Chem.* 2005;280:9308–9312.
12. Mitra R, Morad M. Two types of calcium channels in guinea pig ventricular myocytes. *Proc Natl Acad Sci U S A.* 1986;83:5340–5344.
13. Hoppe UC, Johns DC, Marban E, O'Rourke B. Manipulation of cellular excitability by cell fusion: effects of rapid introduction of transient outward K^+ current on the guinea pig action potential. *Circ Res.* 1999; 84:964–972.
14. Subramaniam A, Jones WK, Gulick J, Wert S, Neumann J, Robbins J. Tissue-specific regulation of the alpha-myosin heavy chain gene promoter in transgenic mice. *J Biol Chem.* 1991;266:24613–24620.
15. Beguin P, Mahalakshmi RN, Nagashima K, Cher DH, Ikeda H, Yamada Y, Seino Y, Hunziker W. Nuclear sequestration of beta-subunits by Rad and Rem is controlled by 14-3-3 and calmodulin and reveals a novel mechanism for Ca^{2+} channel regulation. *J Mol Biol.* 2006;355:34–46.
16. Finlin BS, Crump SM, Satin J, Andres DA. Regulation of voltage-gated calcium channel activity by the Rem and Rad GTPases. *Proc Natl Acad Sci U S A.* 2003;100:14469–14474.
17. Shimizu W, Noda T, Takaki H, Kurita T, Nagaya N, Satomi K, Suyama K, Aihara N, Kamakura S, Sunagawa K, Echigo S, Nakamura K, Ohe T, Towbin JA, Napolitano C, Priori SG. Epinephrine unmasks latent mutation carriers with LQT1 form of congenital long-QT syndrome. *J Am Coll Cardiol.* 2003;41:633–642.
18. Paavonen KJ, Swan H, Piippo K, Hokkanen L, Laitinen P, Viitasalo M, Toivonen L, Kontula K. Response of the QT interval to mental and physical stress in types LQT1 and LQT2 of the long QT syndrome. *Heart.* 2001;86:39–44.
19. Wei L, Taffet GE, Khoury DS, Bo J, Li Y, Yatani A, Delaughter MC, Klevitsky R, Hewett TE, Robbins J, Michael LH, Schneider MD, Entman ML, Schwartz RJ. Disruption of Rho signaling results in progressive atrioventricular conduction defects while ventricular function remains preserved. *FASEB J.* 2004;18:857–859.
20. Simon AM, Goodenough DA, Paul DL. Mice lacking connexin40 have cardiac conduction abnormalities characteristic of atrioventricular block and bundle branch block. *Curr Biol.* 1998;8:295–298.
21. Noma K, Oyama N, Liao JK. Physiological role of ROCKs in the cardiovascular system. *Am J Physiol Cell Physiol.* 2006;290:C661–C668.
22. Pereira L, Matthes J, Schuster I, Valdivia HH, Herzig S, Richard S, Gomez AM. Mechanisms of $[Ca^{2+}]i$ transient decrease in cardiomyopathy of db/db type 2 diabetic mice. *Diabetes.* 2006;55:608–615.
23. Casis O, Echevarria E. Diabetic cardiomyopathy: electromechanical cellular alterations. *Curr Vasc Pharmacol.* 2004;2:237–248.
24. Rossing P, Breum L, Major-Pedersen A, Sato A, Winding H, Pietersen A, Kastrup J, Parving HH. Prolonged QTc interval predicts mortality in patients with type 1 diabetes mellitus. *Diabet Med.* 2001;18:199–205.
25. Wang DW, Kiyosue T, Shigematsu S, Arita M. Abnormalities of K^+ and Ca^{2+} currents in ventricular myocytes from rats with chronic diabetes. *Am J Physiol.* 1995;269:H1288–H1296.
26. Moss FJ, Viard P, Davies A, Bertaso F, Page KM, Graham A, Canti C, Plumpton M, Plumpton C, Clare JJ, Dolphin AC. The novel product of a five-exon stargazin-related gene abolishes Ca,2.2 calcium channel expression. *EMBO J.* 2002;21:1514–1523.
27. Chen H, Puhl HL 3rd, Niu SL, Mitchell DC, Ikeda SR. Expression of Rem2, an RGK family small GTPase, reduces N-type calcium current without affecting channel surface density. *J Neurosci.* 2005;25: 9762–9772.
28. Finlin BS, Correll RN, Pang C, Crump SM, Satin J, Andres DA. Analysis of the complex between Ca^{2+} channel β-subunit and the Rem GTPase. *J Biol Chem.* 2006;281:23557–23566.

nature medicine

Sema3a maintains normal heart rhythm through sympathetic innervation patterning

Masaki Ieda[1,2], Hideaki Kanazawa[1,2], Kensuke Kimura[1], Fumiyuki Hattori[1], Yasuyo Ieda[1], Masahiko Taniguchi[3], Jong-Kook Lee[4], Keisuke Matsumura[1,2], Yuichi Tomita[1], Shunichiro Miyoshi[2], Kouji Shimoda[5], Shinji Makino[1], Motoaki Sano[1], Itsuo Kodama[4], Satoshi Ogawa[2] & Keiichi Fukuda[1]

Sympathetic innervation is critical for effective cardiac function. However, the developmental and regulatory mechanisms determining the density and patterning of cardiac sympathetic innervation remain unclear, as does the role of this innervation in arrhythmogenesis. Here we show that a neural chemorepellent, Sema3a, establishes cardiac sympathetic innervation patterning. Sema3a is abundantly expressed in the trabecular layer in early-stage embryos but is restricted to Purkinje fibers after birth, forming an epicardial-to-endocardial transmural sympathetic innervation patterning. *Sema3a*$^{-/-}$ mice lacked a cardiac sympathetic innervation gradient and exhibited stellate ganglia malformation, which led to marked sinus bradycardia due to sympathetic dysfunction. Cardiac-specific overexpression of *Sema3a* in transgenic mice (*SemaTG*) was associated with reduced sympathetic innervation and attenuation of the epicardial-to-endocardial innervation gradient. *SemaTG* mice demonstrated sudden death and susceptibility to ventricular tachycardia, due to catecholamine supersensitivity and prolongation of the action potential duration. We conclude that appropriate cardiac Sema3a expression is needed for sympathetic innervation patterning and is critical for heart rate control.

Cardiac tissues are extensively innervated by autonomic nerves. The cardiac sympathetic nerves extend from the sympathetic neurons in stellate ganglia, which reside bilateral to the vertebrae. Previous studies have established regional differences in the sympathetic innervation of the heart in larger mammals[1,2]. Sympathetic nerve fibers project from the base of the heart into the myocardium and are located predominantly in the subepicardium in the ventricle[3,4]. The central conduction system, including the sinoatrial node, the atrioventricular node and the His bundle, is abundantly innervated as compared with the working myocardium[1,4–6]. The sympathetic nervous system augments cardiac performance by increasing heart rate, conduction velocity, myocardial contraction, and relaxation. Accordingly, unbalanced neural activation or suppression might trigger lethal arrhythmia in diseased hearts[7–10]. These findings have demonstrated that sympathetic innervation patterning is critical for effective cardiac performance; however, little is known about the developmental and regulatory mechanisms underlying cardiac sympathetic innervation patterning. Moreover, the consequence of its disruption remains unknown.

We and others have reported that nerve growth factor (NGF), a member of the neurotrophin family, is required for sympathetic axon growth and innervation in the heart[11,12]. However, the neural chemorepellent that induces growth cone collapse and repels sympathetic axons in the heart has not been identified. Sema3a is a class 3 secreted semaphorin and a potent neural chemorepellent for sensory and sympathetic axons[13–15]. Targeted inactivation of *Sema3a* disrupts neural patterning and projections, indicating the importance of Sema3a signaling for directional guidance of nerve fibers[16,17]. It remains unknown, however, whether cardiomyocytes produce Sema3a, and, if so, whether this protein affects sympathetic neural patterning and cardiac performance. Here we demonstrate the expression pattern of Sema3a in developing hearts and its critical roles in cardiac sympathetic innervation patterning and arrhythmia, using various gene-modified mouse models.

RESULTS

Sympathetic nerve distribution in mouse heart

We first analyzed the distribution of cardiac sympathetic nerves in adult mouse hearts at postnatal day (P) 42 by immunostaining with an antibody to tyrosine hydroxylase, a marker of sympathetic nerves. Tyrosine hydroxylase–immunopositive (TH^+) nerves were most abundant in the sinoatrial node, the atrioventricular node and the His bundle, as indicated by acetyl cholinesterase (AChE) activity staining (refs. 18,19 and **Fig. 1a**). In contrast, TH^+ nerves in Purkinje

[1]Department of Regenerative Medicine and Advanced Cardiac Therapeutics, Keio University School of Medicine, 35 Shinanomachi, Shinjuku-ku, Tokyo 160-8582, Japan. [2]Cardiology Division, Department of Medicine, Keio University School of Medicine, 35 Shinanomachi, Shinjuku-ku, Tokyo 160-8582, Japan. [3]Department of Biochemistry, Cancer Research Institute, Sapporo Medical University School of Medicine, S-1, W-17, Chuo-ku, Sapporo 060-8556, Japan. [4]Department of Cardiovascular Research, Research Institute of Environmental Medicine, Nagoya University, Furo-cho, Chikusa-ku, Nagoya 464-8601, Japan. [5]Laboratory Animal Center, Keio University School of Medicine, 35 Shinanomachi, Shinjuku-ku, Tokyo 160-8582, Japan. Correspondence should be addressed to K.F. (kfukuda@sc.itc.keio.ac.jp).

Received 9 November 2006; accepted 27 February 2007; published online 8 April 2007; doi:10.1038/nm1570

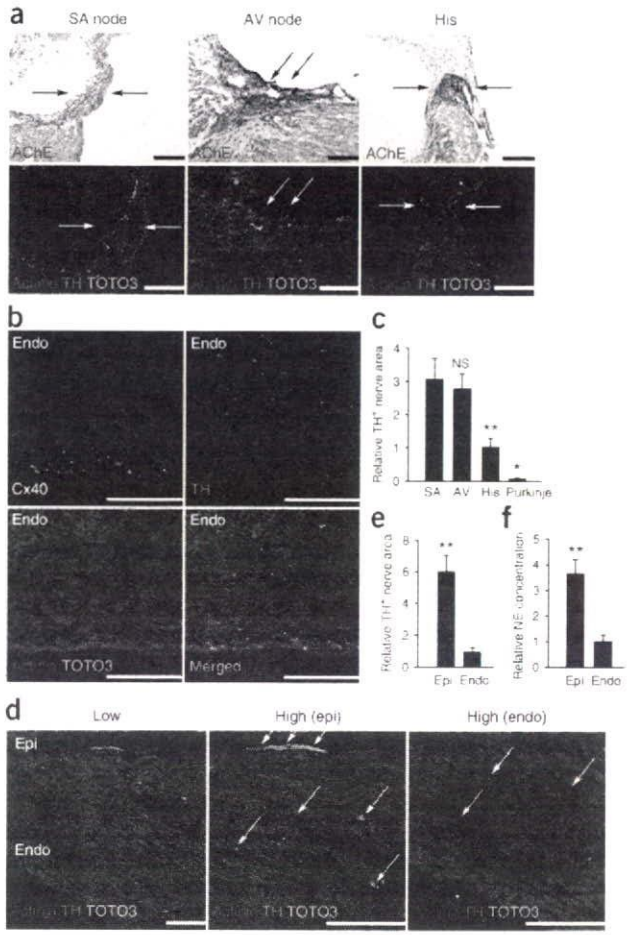

Figure 1 Regional heterogeneity of sympathetic innervation in the mouse heart. (**a**) The sinoatrial (SA) node, atrioventricular (AV) node and His bundle (arrows) stained with AChE (brown) were abundantly innervated by tyrosine hydroxylase–positive (TH^+) nerves. Top, acetyl cholinesterase (AChE) and hematoxylin staining. Bottom, immunofluorescent staining for α-actinin, tyrosine hydroxylase (TH) and TOTO3 (as a nuclear stain). (**b**) Immunofluorescent staining for α-actinin, TH, Cx40 and TOTO3 was performed. Few TH^+ nerves were detected in Purkinje fibers. (**c**) Quantitative analysis of TH^+ nerve areas ($n = 4$). (**d**) Immunofluorescent staining for α-actinin, TH and TOTO3. 'Low' and 'high' indicate low- and high-power fields, respectively. TH^+ nerves (arrows) were more abundant in the subepicardium (epi) than in the subendocardium (endo); quantitative data are shown in **e** ($n = 4$). (**f**) Cardiac norepinephrine (NE) concentration measured by high-performance liquid chromatography (HPLC) ($n = 6$). $^*P < 0.001$; $^{**}P < 0.01$; NS, not significant (in **c**, compared to SA). Scale bars, 100 μm.

fibers, which express connexin40 (Cx40)[20], were barely detectable and present in much smaller numbers than in the surrounding working myocardium (**Fig. 1b,c**). In the ventricular myocardium, TH^+ nerves were abundant and more so in the subepicardium than the subendocardium (**Fig. 1d,e**). The norepinephrine concentration was also significantly higher in the subepicardium (3.7-fold; **Fig. 1f**).

We next analyzed the time course of cardiac sympathetic innervation in developing mouse ventricles. Nerve endings appeared at embryonic day (E) 15 in the epicardial surface and were apparent in the myocardium at P7 and P42 (**Supplementary Fig. 1** online). Together, these results show that cardiac sympathetic nerve density exhibits regional differences, and that sympathetic nerve fibers in mice develop from the epicardial base of the heart into the myocardium, as observed in larger mammals[1,2,5].

Sema3a expression is inversely related to sympathetic innervation

To test whether Sema3a might be a signal for determining cardiac sympathetic innervation patterning, we analyzed heterozygous *Sema3a* knocked-in *lacZ* mice (*Sema3a*$^{lacZ/+}$) and determined *Sema3a* expression in the heart[16]. At E10, we observed *lacZ* expression in the forelimb buds and somites and weakly in the heart. *In situ* hybridization for *Sema3a* confirmed that *lacZ* expression in *Sema3a*$^{lacZ/+}$ mice correctly reflected endogenous gene expression (**Fig. 2a**). At E12, we detected strong *lacZ* expression in the heart, especially in the trabecular component of both ventricles (**Fig. 2b**). In E15 hearts, we observed *lacZ* expression at the subendocardium but not at the subepicardium in the atria and ventricles. At P1 and P42, *lacZ* expression was reduced in certain locations and highlighted the Purkinje fiber network along the ventricular free wall (**Fig. 2c**). To verify the presence of $lacZ^+$ cells in Purkinje fibers at P42, we immunostained sections with an antibody to Cx40 and found that ventricular subendocardial $lacZ^+$ cells also stained for Cx40 (**Fig. 2d**). In contrast, richly innervated and AChE-positive sinoatrial nodes (data not shown), atrioventricular nodes and His bundles did not express *lacZ* (**Fig. 2e**).

Quantitative RT-PCR of *Sema3a* in developing hearts also revealed that *Sema3a* mRNA was present from E12 and its levels then decreased in a linear fashion, in contrast to the sympathetic innervation (**Fig. 2f**). At P42, *Sema3a* mRNA expression was 2.3-fold higher in the subendocardium than in the subepicardium (**Fig. 2g**). These results indicated that *Sema3a* expression has an opposite time course and distribution from sympathetic innervation in developing hearts. Double staining with tyrosine hydroxylase and 5-bromo-4-chloro-3-indolyl-β-D-galactopyranoside (X-gal) revealed that most sympathetic nerves were restricted to the subepicardium at P1, when *Sema3a* was expressed extensively at the midcardial and subendocardial layers. At P42, sympathetic innervation extended vigorously into the ventricular myocardium, concomitant with *Sema3a* being downregulated and confined only to Purkinje fibers (**Fig. 2h**). Together, these results suggested that *Sema3a* is synthesized in Purkinje fibers and its expression is inversely related to the extent of sympathetic innervation.

Innervation patterning is disrupted in *Sema3a*$^{-/-}$ hearts

To investigate whether Sema3a is critical for cardiac sympathetic nerve development, we analyzed *Sema3a* homozygous null mice (*Sema3a*$^{-/-}$)[16]. Most *Sema3a*$^{-/-}$ mice die within the first postnatal week, and only 20% remain viable until weaning[16,17]. At P1, thick and fasciculated nerve fibers were restricted to the epicardial surface and few fibers were detected within the myocardium in the hearts of wild-type mice. In *Sema3a*$^{-/-}$ hearts, only a few fibers were observed at the epicardial surface, but many axons projected aberrantly into the myocardium at this early stage (**Fig. 3a,b**). To examine the overall pattern of cardiac sympathetic innervation, we performed whole-mount immunostaining for tyrosine hydroxylase at P1 on wild-type and *Sema3a*$^{-/-}$ hearts. Sympathetic nerve fibers appeared thinner and were fewer in number on the epicardial surface of *Sema3a*$^{-/-}$ hearts (**Fig. 3c**). At P14, when the sympathetic nerves extended into the myocardium, wild-type hearts showed a clear epicardial-to-endocardial gradient of sympathetic innervation. In contrast, sympathetic nerve density was reduced in the subepicardium but increased

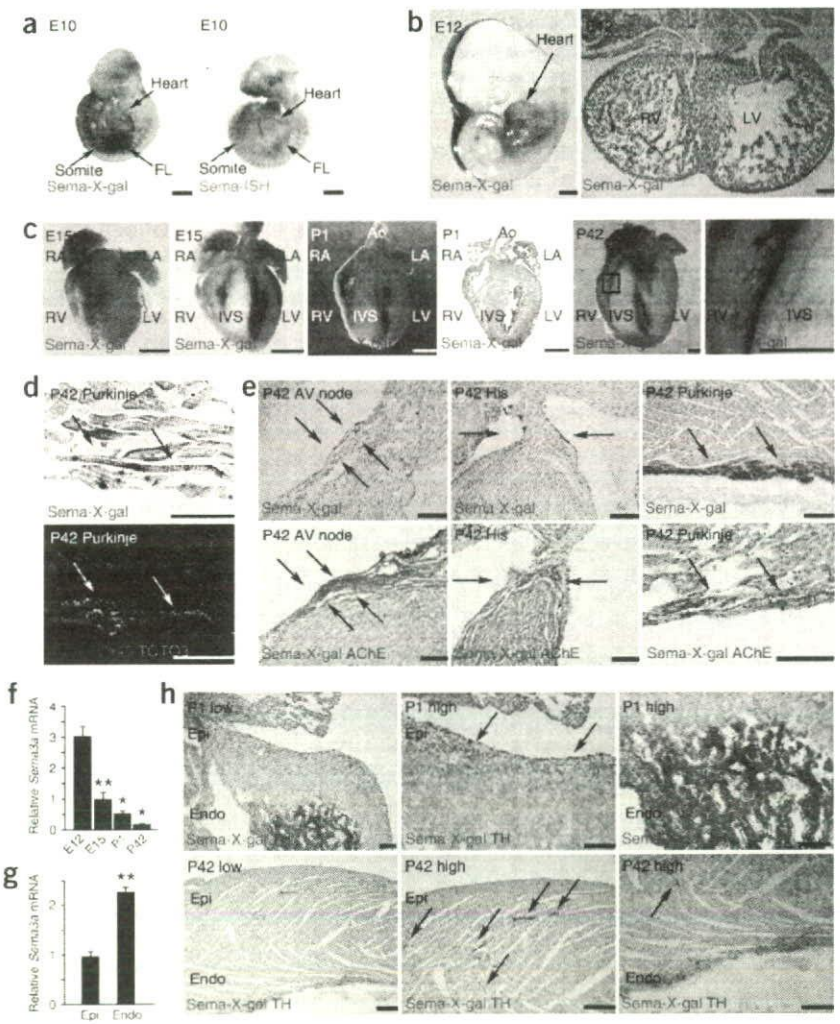

Figure 2 Inverse pattern of *Sema3a* expression and sympathetic innervation in developing hearts. (**a**) X-gal staining (green) of *Sema3a*$^{lacZ/+}$ at E10 (left). *In situ* hybridization (ISH) for *Sema3a* (right). (**b**) X-gal staining of *Sema3a*$^{lacZ/+}$ at E12 demonstrated strong *Sema3a* expression in the heart. (**c**) *lacZ* expression was observed in the subendocardium in *Sema3a*$^{lacZ/+}$ hearts at E15. The signal-positive areas were gradually reduced by P1 and P42, and a higher magnification view of the network of Purkinje fibers in P42 *Sema3a*$^{lacZ/+}$ hearts is shown in the far right micrograph. (**d**) X-gal staining (top) and triple immunofluorescence staining for α-actinin, Cx40 and TOTO3 (bottom) in the subendocardium in P42 *Sema3a*$^{lacZ/+}$ hearts. Arrows indicate Purkinje fibers demarcated with Cx40. (**e**) X-gal staining (top), and double staining with AChE (brown) and X-gal (blue) (bottom) for the conduction system (arrows) in P42 *Sema3a*$^{lacZ/+}$ hearts. Note that AChE-positive AV node and His bundle did not express *lacZ*, but AChE-positive Purkinje fibers were colabeled with X-gal staining. (**f**) *Sema3a* mRNA expression in wild-type developing hearts determined by quantitative RT-PCR ($n = 5$). (**g**) *Sema3a* expression in the subendocardium and subepicardium in wild-type mice ($n = 5$). (**h**) Double staining with tyrosine hydroxylase (TH, brown) and X-gal (blue) in P1 and P42 *Sema3a*$^{lacZ/+}$ hearts. 'Low' and 'high' indicate low and high magnification, respectively. Note that sympathetic nerves were restricted to the subepicardium at P1, but extended into the myocardium at P42, coincident with downregulation of Sema3a. Representative data are shown in **a**–**e** and **h**. $^*P < 0.001$ and $^{**}P < 0.01$ (in **f**, compared to data at E12). FL, forelimb; RA, right atrium; LA, left atrium; RV, right ventricle; LV, left ventricle; IVS, interventricular septum; Ao, aorta. Scale bars: 50 μm in **d**; 100 μm in the right panel of **b**; 100 μm in **e**,**h**; 1 mm in all others.

in the subendocardium in *Sema3a*$^{-/-}$ mice, resulting in a marked reduction of the subepicardial-to-subendocardial ratio of sympathetic innervation (7.7-fold in wild-type and 0.8-fold in *Sema3a*$^{-/-}$ animals **Fig. 3d–f**).

Next, we performed double staining with X-gal and tyrosine hydroxylase in *Sema3a*$^{lacZ/+}$ (*Sema3a* heterozygous null) and *Sema3a*$^{lacZ/lacZ}$ (*Sema3a* homozygous null) hearts. *Sema3a*$^{lacZ/+}$ hearts showed a restricted sympathetic innervation within the working myocardium, and the axons never extended into the *Sema3a*-expressing Purkinje fibers. In *Sema3a*$^{lacZ/lacZ}$ hearts, we observed many aberrant projections at the subendocardium where *lacZ* was expressed, and sympathetic nerves grew freely over *lacZ*-expressing areas (**Fig. 3g**). These results indicated that Sema3a is critical for the patterning of cardiac sympathetic innervation.

Sema3a$^{-/-}$ mice exhibit sinus bradycardia

We next examined the central conduction system in *Sema3a*$^{-/-}$ hearts. The sinoatrial nodes, atrioventricular nodes and His bundles, demarcated with AChE activity staining, were intact in appearance in *Sema3a*$^{-/-}$ hearts. The sympathetic nerve density in the conduction system was also not different between wild-type and *Sema3a*$^{-/-}$ hearts (**Fig. 4a** and **Supplementary Fig. 2** online). To determine whether sympathetic neurons that project nerve fibers to the heart were disrupted, we examined the stellate ganglia. TH$^+$ neurons accumulated to form sympathetic ganglia at positions bilateral to the vertebrae in wild type mice. In contrast, the sympathetic neurons did not accumulate in *Sema3a*$^{-/-}$ mice but instead were distributed widely in a dislocated pattern (**Fig. 4b**). The stellate ganglia malformation was sustained at P42 in *Sema3a*$^{-/-}$ mice (data not shown).

To identify the effects of abnormal sympathetic neural distribution in the absence of Sema3a expression, we performed telemetric electrocardiography (ECG) in awake and free-moving wild-type and *Sema3a*$^{-/-}$ mice ($n = 5$ in both groups), of age 6 to 8 weeks. *Sema3a*$^{-/-}$ mice showed sinus bradycardia and abrupt sinus slowing, with a heart rate of 531 ± 27 beats per min compared with 604 ± 36 beats per min in wild-type mice (**Fig. 4c** and **Supplementary Table 1** online). To determine whether the bradycardia arose from intrinsic or extrinsic defects in the sinus node, we measured heart rate responses following pharmacological intervention. Blocking the sympathetic system with propranolol reduced the heart rate to a larger extent in the wild-type mice than in *Sema3a*$^{-/-}$ mice, suggesting that basal sympathetic activity was downregulated in *Sema3a*$^{-/-}$ hearts. In contrast, blocking parasympathetic activity had no substantial effect in either group of mice, consistent with previous reports showing that mice have weak

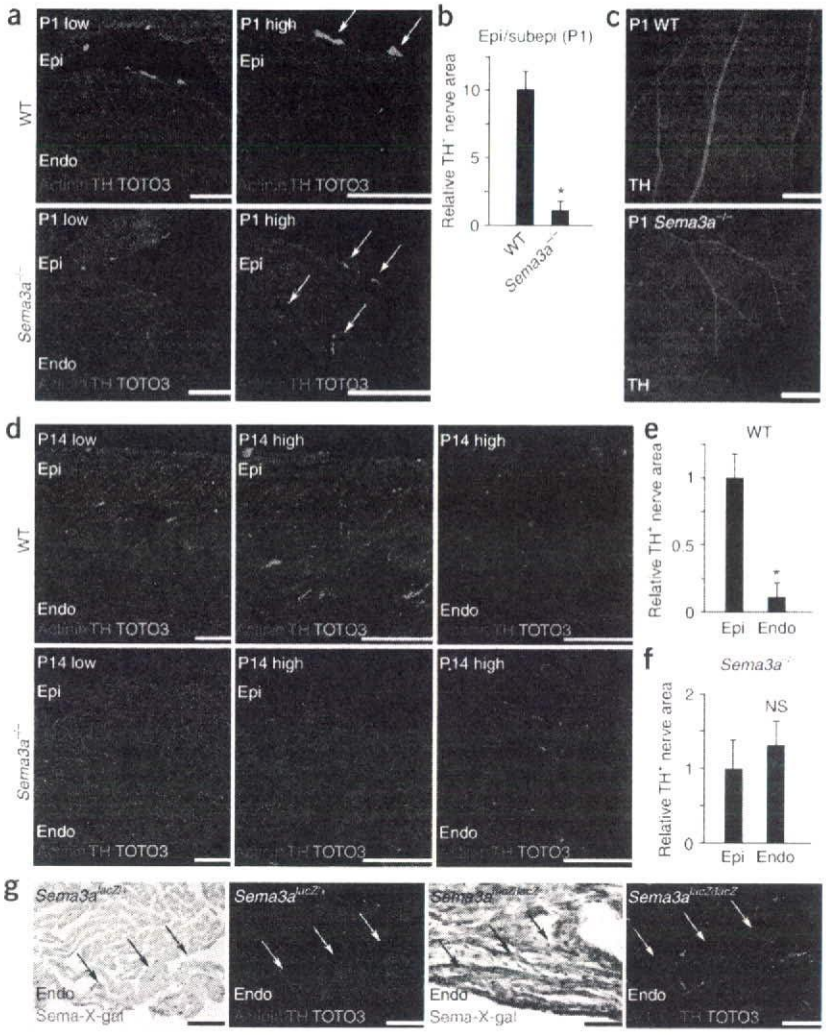

Figure 3 Cardiac sympathetic innervation patterning is disrupted in *Sema3a*-deficient mice. (**a**) Triple immunostaining for α-actinin, tyrosine hydroxylase (TH) and TOTO3 in P1 wild-type and *Sema3a*$^{-/-}$ hearts (low- and high-power fields). Arrows indicate sympathetic nerves. (**b**) Quantitative analysis of TH$^+$ nerve area in the epicardium and subepicardium in wild-type (WT) and *Sema3a*$^{-/-}$ hearts at P1 ($n = 5$). (**c**) Whole-mount immunofluorescence staining for TH in wild-type and *Sema3a*$^{-/-}$ hearts at P1. (**d**) Triple immunostaining for α-actinin, TH and TOTO3 in P14 wild-type and *Sema3a*$^{-/-}$ hearts (low- and high-power fields). An epicardial-to-endocardial gradient of sympathetic innervation was observed in wild-type hearts, but not in *Sema3a*$^{-/-}$ hearts, at P14. (**e**,**f**) Quantitative analysis of TH$^+$ nerve area in the subepicardium and subendocardium in wild-type and *Sema3a*$^{-/-}$ mice at P14 ($n = 5$). (**g**) Comparisons between X-gal and TH staining in P14 *Sema3a*$^{lacZ/+}$ and *Sema3a*$^{lacZ/lacZ}$ hearts are shown. Many aberrant nerves were observed in the *lacZ*-expressing area only in *Sema3a*$^{lacZ/lacZ}$ hearts (*Sema3a* homozygous null). Arrows indicate the *Sema3a*-expressing area visualized by *lacZ* expression. Representative data are shown in **a**,**c**,**d** and **g**. $^*P < 0.01$; NS, not significant. Scale bars, 100 μm.

parasympathetic activity[21,22]. The intrinsic heart rate, determined by blocking both autonomic activities, was not different between the two groups, suggesting that *Sema3a*$^{-/-}$ hearts retained intrinsic sinus node function (**Fig. 4d**). To further elucidate the autonomic activities, we performed a heart rate variability (HRV) analysis. Spectral analysis revealed a significant reduction in normalized low filtration (NLF) and in the low-to-high filtration (LF-to-HF) ratio (markers of sympathetic activity) and an increase in normalized high filtration (NHF) in *Sema3a*$^{-/-}$ mice (**Fig. 4e–g**). Thus, the intrinsic sinus node function (a cell-autonomous effect) was preserved, but sympathetic neural activity (a cell-non-autonomous effect) was significantly downregulated in *Sema3a*$^{-/-}$ hearts, presumably owing to malformation of sympathetic ganglia. These results indicated that *Sema3a*$^{-/-}$ mice develop sinus bradycardia as a result of sympathetic neural dysfunction. *Sema3a*$^{-/-}$ mice also showed spontaneous premature ventricular contractions (PVCs) (*Sema3a*$^{-/-}$: 2 of 10 mice; wild-type: 0 of 10 mice) (**Fig. 4h**). However, sustained ventricular tachycardia was not observed in either group before or after epinephrine injection.

Cardiac-specific *Sema3a* overexpression reduces innervation

It is possible that the abnormal patterning of cardiac sympathetic nerves in *Sema3a*-deficient hearts was a secondary effect of the malformation of sympathetic ganglia. To address this, we generated cardiac-specific transgenic mice expressing *Sema3a* (*SemaTG*) under the control of an α-myosin heavy chain promoter[23]. Northern blot analysis revealed that *Sema3a* was expressed exclusively in the heart. The expression of other factors known to be involved in sympathetic innervation, such as NGF and vascular endothelial growth factor-A, was unaffected in *SemaTG* mice (**Fig. 5a**). The growth cone collapse assay revealed that media conditioned with *SemaTG* cardiomyocytes had strong chemorepellent effects on sympathetic nerves, indicating that bioactive Sema3a was secreted from *SemaTG* cardiomyocytes (refs. 24,25 and **Fig. 5b**). *In situ* hybridization for *Sema3a* demonstrated *Sema3a* expression only at the subendocardium, not at the mid- or subepicardium, in wild-type hearts, similar to the results for *Sema3a*$^{lacZ/+}$ hearts. In contrast, *Sema3a* was expressed throughout the ventricles in *SemaTG* mice and showed higher expression at the subendocardium and midcardium than at the subepicardium in the ventricles. There was no *Sema3a* expression in the atrioventricular nodes or His bundles in either genotype (**Fig. 5c** and **Supplementary Fig. 3** online). Echocardiography and histology did not identify any contractile dysfunction or structural defects in *SemaTG* hearts.

To determine whether sympathetic innervation was altered in *SemaTG* mice, we immunostained mouse hearts with an antibody to tyrosine hydroxylase and measured the norepinephrine concentration in the ventricles (**Fig. 5d**,**e** and **Supplementary Fig. 3**). In *SemaTG* ventricles, sympathetic innervation was markedly reduced and the total cardiac norepinephrine concentration was reduced by 76%. Sympathetic innervation of the sinoatrial nodes, atrioventricular nodes and His bundles was not altered in *SemaTG* hearts (data not shown). We next analyzed the transmural difference of sympathetic innervation in *SemaTG* hearts. TH$^+$ nerve fibers and norepinephrine

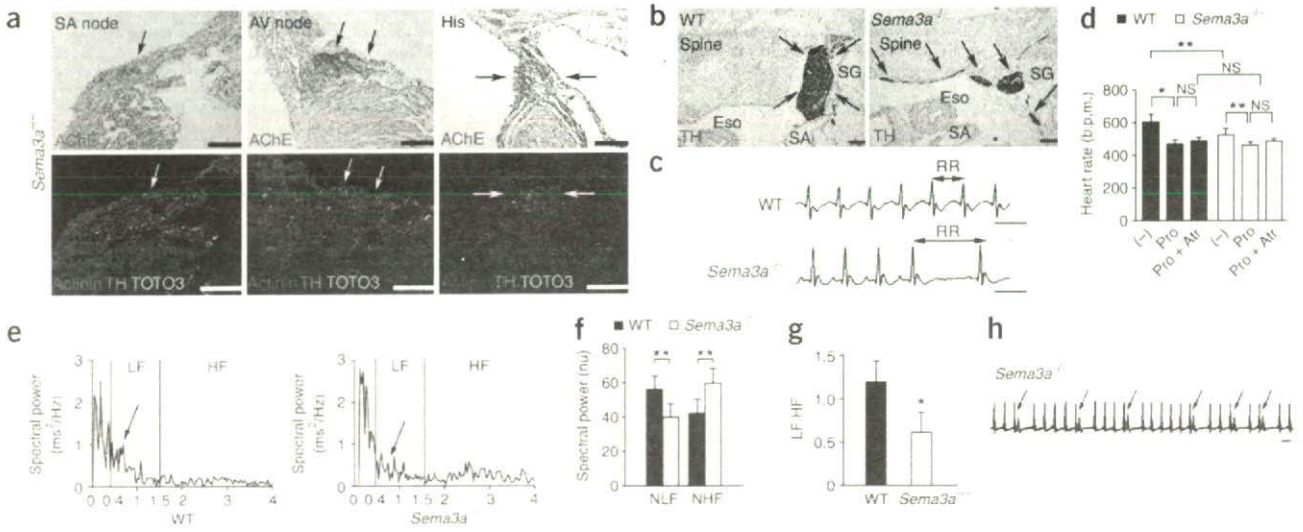

Figure 4 *Sema3a*-deficient mice display malformation of stellate ganglia and sinus bradycardia. (**a**) Top, AChE (brown) and hematoxylin (purple) staining. Bottom, immunostaining of sinoatrial node, atrioventricular node and His bundle (arrows) in P14 *Sema3a*$^{-/-}$ hearts with α-actinin, tyrosine hydroxylase (TH) and TOTO3. (**b**) Stellate ganglia (SG, arrows) in P1 animals were observed by TH immunostaining (brown). Note that a single SG was observed at a position lateral to the spine in wild-type mice, but that multiple SG were distributed widely in a dislocated pattern in *Sema3a*$^{-/-}$ mice Eso, esophagus; SA, subclavian artery. (**c**) ECG recordings from wild-type and *Sema3a*$^{-/-}$ mice. The lengthened RR interval indicates abrupt sinus slowing in *Sema3a*$^{-/-}$ mice. (**d**) Changes in heart rate following pharmacological modifications in wild-type and *Sema3a*$^{-/-}$ mice ($n = 5$). Note that propranolol reduced heart rate to a lesser extent in *Sema3a*$^{-/-}$ mice than in wild-type mice. (–), no addition; Pro, propranolol; Pro + Atr, propranolol + atropine. (**e**) Power spectra of heart-rate variability (HRV) in wild-type and *Sema3a*$^{-/-}$ mice. Note decrease of HRV across low filtration (LF) band in *Sema3a*$^{-/-}$ mice, reflecting lower sympathetic nerve activity (arrows). (**f**,**g**) The normalized low filtration (NLF) and the low-to-high filtration (LF:HF) ratio were decreased in *Sema3a*$^{-/-}$ mice ($n = 5$). (**h**) Spontaneous and frequent premature ventricular contractions (PVCs, arrows) were observed in *Sema3a*$^{-/-}$ mice. Representative data are shown in **a**–**c**, **e** and **h**. $^{*}P < 0.01$; $^{**}P < 0.05$; NS, not significant. Scale bars: 100 μm in **a**,**b**; 100 ms in **c**,**h**.

concentration were decreased proportionally at both the subepicardium and subendocardium in *SemaTG* ventricles (**Fig. 5f,g**). Therefore, sympathetic innervation density was inversely proportional to *Sema3a* expression in *SemaTG* hearts. The appearance of stellate ganglia was not different between wild-type and *SemaTG* mice (**Fig. 5h**). These results indicated that cardiomyocyte-derived Sema3a mediates repulsive and inhibitory effects on cardiac sympathetic neural growth.

SemaTG mice are susceptible to ventricular arrhythmias

The *SemaTG* mice died suddenly, without any symptoms, at 10 months of age (4 of 22 *SemaTG* mice versus 0 of 22 wild-type mice) (**Fig. 6a**), and necropsy showed no abnormalities. Telemetry ECG revealed spontaneous PVCs in *SemaTG* mice but not in wild-type mice (3 of 10 *SemaTG* mice versus 0 of 10 wild-type mice), whereas there were no significant differences in other ECG parameters (**Fig. 6b** and **Supplementary Table 2** online). Epinephrine administration induced multiple nonsustained and sustained episodes of ventricular tachycardia in the *SemaTG* mice only (2 of 10 *SemaTG* mice versus 0 of 10 wild-type mice) (**Fig. 6c**). To further characterize susceptibility to arrhythmia, we subjected wild-type and *SemaTG* mice to programmed electrical stimulation. *SemaTG* mice had nonsustained ventricular tachycardia at baseline, the frequency and duration of which were significantly increased by a low dose of isoproterenol (**Fig. 6d,e**; 8 of 10 *SemaTG* mice). In contrast, no wild-type mice ($n = 10$) developed sustained ventricular tachycardia. There were no electrophysiological differences between the two groups (**Supplementary Table 2**).

It is possible that the hypoinnervated *SemaTG* hearts showed ventricular arrhythmias as a result of catecholamine supersensitivity. To test this possibility, we measured cyclic AMP (cAMP) levels in wild-type and *SemaTG* ventricles before and after isoproterenol injection. Although basal cAMP levels were not different, the increase in cAMP after isoproterenol administration was greater in *SemaTG* mice than wild-type mice, indicating an augmented adrenergic response in *SemaTG* hearts (**Fig. 6f**). To investigate this mechanistically, we measured the density of the β_1-adrenergic receptor (β_1AR) in the ventricles. The β_1AR density was 1.5-fold greater in *SemaTG* ventricles (**Fig. 6g**).

We next investigated the transmembrane action potential of left ventricular myocytes, using glass microelectrodes. Action potential duration (APD) assessed at 50% and 90% repolarization (APD_{50} and APD_{90}) were shorter in the subepicardium than in the subendocardium in the wild-type mice. APD was significantly prolonged in hypoinnervated *SemaTG* subepicardium and subendocardium, and was inversely proportional to sympathetic innervation density. The action potential amplitude, resting membrane potential and maximum positive deflection of phase 0 upstroke were not altered, indicating that repolarization currents were disrupted in *SemaTG* hearts (**Fig. 6h**). These results suggested that the higher susceptibility of *SemaTG* mice to ventricular arrhythmia was due to catecholamine supersensitivity and APD prolongation, both of which might augment triggered activity in cardiomyocytes.

DISCUSSION

This work shows that a gradient of the neural chemorepellent Sema3a is essential for proper cardiac sympathetic innervation patterning, and that inappropriate Sema3a expression triggers various kinds of arrhythmias as a result of the disruption of this patterning. To our knowledge, this is the first identification of a critical regulatory

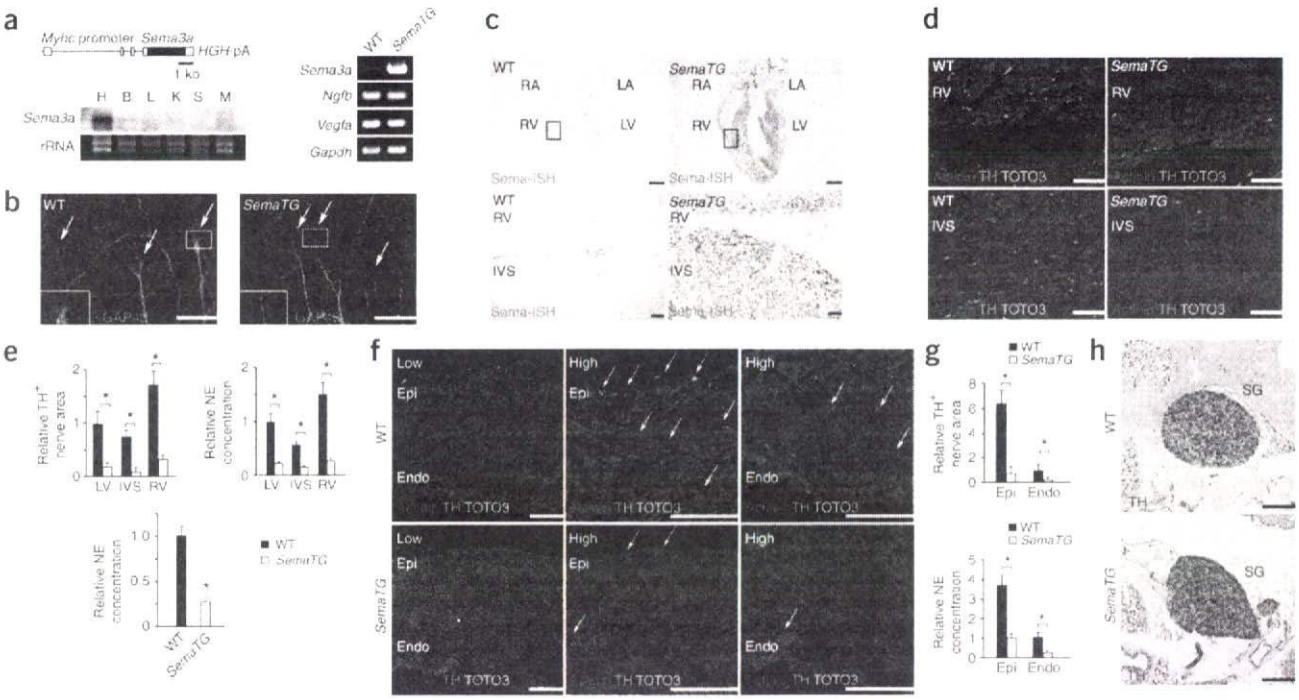

Figure 5 Cardiac sympathetic innervation patterning was disturbed in *SemaTG* hearts. (**a**) Schematic representation of the transgene containing the α-myosin heavy chain (*Myhc*) promoter, mouse *Sema3a* cDNA and human growth hormone (*HGH*) polyadenylation signal (pA). Northern blot analysis for *Sema3a* in *SemaTG* mice and RT-PCR analysis of *Sema3a*, *Ngfb*, *Vegfa* and *Gapdh* in wild-type and *SemaTG* hearts are shown. H, heart; B, brain; L, liver; K, kidney; S, spleen; M, muscle. (**b**) Growth cone collapse assay, visualized with GAP43 immunostaining. Arrows indicate growth cones. Insets show high-power views of the boxed areas. (**c**) *In situ* hybridization (ISH) for *Sema3a* in wild-type and *SemaTG* hearts. High-power views of the boxed areas are shown in the lower micrographs. (**d**) Triple immunofluorescence staining for α-actinin, tyrosine hydroxylase (TH) and TOTO3 in wild-type and *SemaTG* hearts. (**e**) TH$^+$ nerve areas were decreased in *SemaTG* hearts ($n = 5$). Cardiac norepinephrine (NE) concentrations were also reduced in *SemaTG* ventricles compared with wild-type ventricles ($n = 8$). (**f**) Triple immunofluorescence staining for α-actinin, TH and TOTO3 in wild-type and *SemaTG* hearts. The number of TH$^+$ nerves was decreased in both the subepicardium (Epi) and the subendocardium (Endo) in *SemaTG* ventricles. Arrows indicate TH$^+$ nerves. (**g**) Quantitative analysis of TH$^+$ nerve area and norepinephrine concentrations in the subepicardium and the subendocardium ($n = 5$). (**h**) Stellate ganglia (SG) were not abnormal in *SemaTG* mice. Representative data are shown in **b**–**d**,**f** and **h**. LV, left ventricle; IVS, interventricular septum; RV, right ventricle; RA, right atrium; LA, left atrium. All mice were analyzed at 6 weeks of age. * $P < 0.01$. Scale bars: 50 μm in **b**,**d**; 100 μm in lower panels of **c**; 100 μm in **f**,**h**; 1 mm in top panels of **c**.

factor for cardiac sympathetic patterning. The expression pattern of Sema3a in the heart is inversely related to sympathetic innervation. Sympathetic nerves express both the NGF receptor TrkA and the Sema3a receptor neuropilin-1 (refs. 14,24). During development, NGF and Sema3a are expressed within the spinal cord and influence pathway guidance of sensory axons. Sema3a is specifically expressed in the ventral half of the spinal cord and induces NGF-responsive sensory axons to terminate at the dorsal part of the spinal cord[13,26]. Thus, the growth cone behavior of sensory axons is modulated by coincident signaling between NGF and Sema3a (ref. 27). As cardiomyocyte-derived NGF acts as a chemoattractant and Sema3a is a potent chemorepellent for sympathetic nerves, it might be the balance between NGF and Sema3a synthesized in the heart that determines cardiac sympathetic innervation patterning. The phenotype of *Sema3a*$^{-/-}$ hearts strongly suggests that no other semaphorin ligands can compensate for loss of *Sema3* function in the control of cardiac sympathetic neural patterning.

Sema3a promotes the aggregation of neurons into sympathetic ganglia during early embryogenesis. This was demonstrated previously with displacement of sympathetic neurons and abnormal morphogenesis of the sympathetic trunk in *Sema3a*$^{-/-}$ mice observed at E12.5 (ref. 14). However, little is known about the role of Sema3a after birth. We found a sustained deficiency in sympathetic neural patterning in *Sema3a*$^{-/-}$ hearts and dislocation of stellate ganglia at P1 and P42. Sympathetic nerve density was inversely proportional to Sema3a expression in *SemaTG* hearts, in which Sema3a is expressed mainly after birth. These results indicate that endogenous Sema3a is crucial for the cardiac sympathetic patterning, not only during embryonic development but also after birth.

Sympathetic nerves modulate the function of ion channels and trigger various types of arrhythmias in diseased hearts[28,29]. However, the relationship between sympathetic innervation and arrhythmogenicity in structurally normal hearts remains unclear. *Sema3a*$^{-/-}$ mice exhibited sinus bradycardia, abrupt sinus slowing and stellate ganglia defects. Pharmacological and HRV analysis confirmed a reduced sympathetic nerve activity in *Sema3a*$^{-/-}$ hearts. Consistent with our results, right stellectomy induces sinus bradycardia and sudden, asystolic death in dogs[30,31]. *SemaTG* hearts were also highly susceptible to ventricular arrhythmias, although without contractile dysfunction or structural defects. Given that catecholamine augments systolic function, it is surprising that *SemaTG* hearts showed normal cardiac function. However, consistent with our results, patients who underwent heart transplantation and had denervated hearts did not show heart failure, whereas about 10% of the patients developed sudden

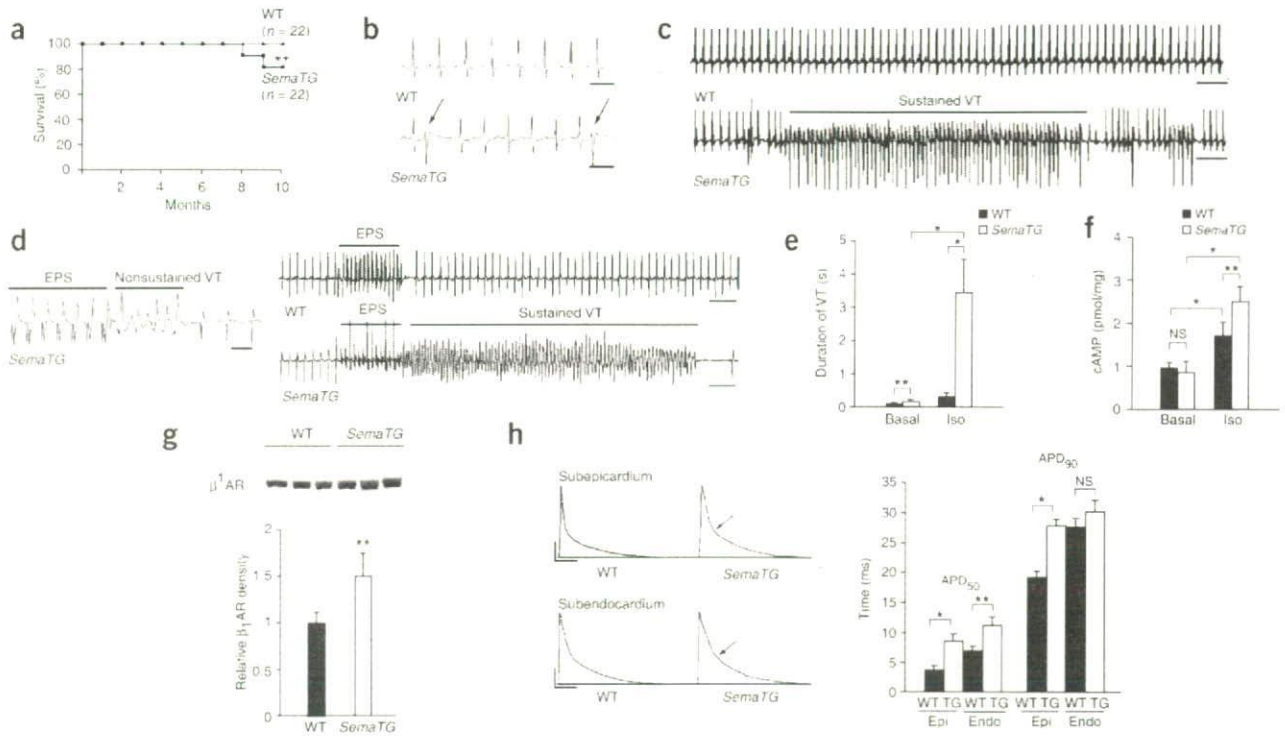

Figure 6 *SemaTG* mice are highly susceptible to induction of ventricular arrhythmia. (**a**) Survival curves of wild-type and *SemaTG* mice. (**b**) Spontaneous PVCs (arrows) were frequently observed in *SemaTG* mice. (**c**) Epinephrine administration revealed sustained ventricular tachycardia (VT) only in *SemaTG* mice. (**d**) Surface ECG during programmed electrical stimulation (EPS) showing nonsustained VT at baseline, and sustained VT after administration of isoproterenol in *SemaTG* mice. The heart was paced epicardially at an S1-S1 interval of 80 ms, followed by a premature beat of 50 ms at an S1-S2 interval. (**e**) Average duration of VT episodes before and after isoproterenol (Iso) ($n = 10$). (**f**) Intracellular concentration of cAMP at basal levels and after isoproterenol administration in wild-type and *SemaTG* hearts ($n = 5$). (**g**) Immunoblotting showed increased β_1AR levels in membrane fractions from *SemaTG* hearts. The relative β_1AR density is shown ($n = 5$). (**h**) Representative action potential tracing from wild-type and *SemaTG* subepicardium (Epi) and subendocardium (Endo). *SemaTG* subepicardium and subendocardium showed prolonged action potentials (arrows). Mean APD measured at 50% and 90% repolarization in wild-type and *SemaTG* (TG) hearts is shown (APD_{50} and APD_{90}; $n = 10$). Representative data are shown in **b**–**d**,**g** and **h**. Mice were analyzed at 6 to 8 weeks of age (**b**–**h**). $^*P < 0.01$; $^{**}P < 0.05$; NS, not significant. Scale bars: 20 ms and 20 mV in **h**; 100 ms in **b** and left panel of **d**; 500 ms in **c** and right panel of **d**.

cardiac death, presumably due to arrhythmias[32]. We also observed similar basal cAMP levels and upregulation of β_1AR in *SemaTG* hearts compared with wild-type hearts. These data therefore strongly support the idea that sympathetic nerves contribute to the fine control of cardiac performance on demand, but not to basal cardiac function. The findings that both the induction of ventricular tachycardia and the production of cAMP were enhanced by isoproterenol, and that *SemaTG* hearts were severely hypoinnervated, implicate adrenergic denervation supersensitivity as a cause of arrhythmogenicity in *SemaTG* mice. It is possible that Sema3a acts directly on cardiomyocytes, but we consider this unlikely, as its receptor neuropilin-1 is expressed in cardiomyocytes only at low levels[33,34]. Action potential duration was inversely proportional to sympathetic innervation density in wild-type and *SemaTG* ventricles, suggesting that sympathetic innervation might regulate repolarization currents. Given that the electrical properties of ventricular myocytes are heterogeneous and that the cardiac repolarization gradient is highly organized through a transmural structure in ventricles[35–37], it would be intriguing to investigate the relationship between sympathetic innervation patterning and the ventricular repolarization gradient.

In conclusion, our results indicate that normal sympathetic innervation patterning mediated by Sema3a is important for the maintenance of arrhythmia-free hearts. Knowledge of the mechanisms regulating sympathetic patterning in hearts may represent a new step toward potential therapies for lethal arrhythmia.

METHODS

Animals. *Sema3a*$^{-/-}$ mice and *Sema3a* knocked-in *lacZ* mice were generated as described previously[16].

Generation of transgenic mice expressing *Sema3a* in the heart. The *Sema3a* cDNA was subcloned into an expression vector containing the α-myosin heavy chain promoter[23]. Pronuclear microinjection and other procedures were performed according to standard protocols of the Keio University Animal Care Center. The transgene was identified by PCR analysis (forward primer, 5′-GTGGTCCACATTCTTCAGGA-3′; reverse primer, 5′-GAGGCAGTCAG TAGTTTGGG-3′). All mice used in this study (*Sema3a*$^{-/-}$, *Sema3a*$^{lacZ/lacZ}$ and *SemaTG*) were backcrossed ten times into the C57BL/6 background. The Keio University Ethics Committee for Animal Experiments approved all experiments in this study.

Northern blot and quantitative RT-PCR. RNA was isolated from several tissues and from left ventricular subepicardial and subendocardial sections. For northern blot analysis, 20 μg of total RNA was used. The *Sema3a* cDNA was obtained from a C57BL/6 adult brain cDNA library as described previously[11]. Quantitative RT-PCR was performed with TaqMan probes (Applied Biosystems): *Sema3a* (Mm00436469_m1) and *Vegfa* (Mm00437304_m1). The

primers and probes for *Ngfb* were as described previously[11]. The mRNA levels were normalized by comparison to *Gapdh* mRNA.

Western blot analysis. Myocardial membrane fractions were prepared by homogenization of hearts in ice-cold buffer as described[38]. Immunodetection was performed on membrane extracts with an antibody to β_1AR (Affinity BioReagents) as previously described[38]. After transfer to nitrocellulose membranes, the 64-kDa β_1AR protein was visualized by chemiluminescence detection (ECL, Amersham).

Detection of growth cone collapse. Stellate ganglia explants were removed from E14 embryos and cultured in medium containing 10% FBS and NGF (Upstate)[39]. After 24 h incubation, the explants were cultured with cardiomyocyte-conditioned media. For detection of growth cone collapse, the cultures were immunostained with an antibody to GAP43 (Chemicon)[25]. Sema3a-Fc (R&D systems) was used as a positive control.

***In situ* hybridization.** *In situ* hybridization with digoxigenin-labeled mouse *Sema3a* antisense cRNA was performed on whole embryos and paraffin-embedded sections[14]. The bound probes were visualized with alkaline phosphatase–conjugated Fab fragment of antibody to digoxigenin (Boehringer Mannheim).

Norepinephrine measurement. Norepinephrine concentration was determined by high-performance liquid chromatography (HPLC) as described previously[11].

Immunohistochemistry of hearts. Hearts were perfused from the apex with 0.4% paraformaldehyde in phosphate-buffered saline, fixed overnight, and then embedded in optimal cutting temperature (OCT) compound and frozen in liquid nitrogen. Hearts were cut longitudinally in 5-μm sections near the central conduction system to show the four chambers. Cryostat sections were stained with antibodies to α-actinin (Sigma Aldrich), connexin40 (Chemicon) and tyrosine hydroxylase (Chemicon) to detect cardiomyocytes, Purkinje fibers and sympathetic nerve fibers, respectively. The sections were incubated with secondary antibodies conjugated with Alexa 488 or 594 (Molecular Probes) and the nuclei were stained with TOTO3 (Molecular Probes). All confocal microscopy was carried out on an LSM 510 META microscope (Carl Zeiss). In some experiments, paraffin-embedded sections were stained with an antibody to tyrosine hydroxylase. Following hybridization with the secondary antibody, sections were incubated with diaminobenzidine. Nerve density was determined as described previously[11]. Briefly, we defined an epicardial portion as an epicardial half of the ventricle and an endocardial portion as an endocardial half of the ventricle for each slide. Within each portion, the six fields that contained the most nerve fiber structures were analyzed. The nerve density was the ratio between the total area of nerves and the total myocardial area, each measured by Image J software. The data for each mouse were calculated from 30 to 40 serial sections. To determine the nerve density in the conduction system, the acetyl cholinesterase–positive or connexin40-positive demarcated areas were analyzed as above. For whole-mount immunostaining, hearts were fixed with 4% paraformaldehyde and stained with an antibody to tyrosine hydroxylase.

Histological analysis. Acetyl cholinesterase staining was performed to localize the central conduction system. For serial sections of the atrioventricular node and the His bundle, anatomical landmarks were used to help guide the decision to begin collection of the sections[18,19].

Electrocardiographic recordings. Telemetric ECG recordings were obtained from conscious adult mice using a wireless implantable transmitter manufactured by Data Sciences International. Mice were anesthetized with ketamine (30 mg/kg) and xylazine (6 mg/kg) and the transmitter was placed in the abdominal cavity. The limb leads were placed in the right arm and the left leg. After implantation of the transmitter, mice were allowed to recover for at least 72 h before data collection. The telemetry data was collected continuously for 2 d and analyzed using HEM 3.4 software (Notocord Systems). Propranolol (4 mg/kg) and atropine (1 mg/kg) were injected intraperitoneally, and changes were examined during 30 min before and after injection[21]. For catecholamine stimulation, epinephrine (2 mg/kg) was injected intraperitoneally[40].

Heart-rate variability (HRV) analysis. HRV analysis was conducted following standard guidelines as described previously[41,42]. Spectral analysis using a fast Fourier transform algorithm on sequences of 512 points was performed using the HEM 3.4 software. The area under the curve was calculated for the very-low-frequency (<0.4 Hz), low-frequency (LF: 0.4–1.5 Hz) and high-frequency (HF: 1.5–4.0 Hz) bands. Spectral variability at each bandwidth was normalized (NLF, NHF) to the total spectral area[41,42].

Electrophysiology. Mice were intubated and anesthetized with 0.5% isofluorane gas, and a surface ECG was recorded during the experiment. After midline sternotomy, a bipolar stimulating electrode was positioned on the left ventricular surface. Standard pacing protocols for electrical stimulation in mice were used[43,44]. Burst pacing and 15 rapid ventricular pacing at cycle lengths of 100 ms and 80 ms with extrastimulation were performed to determine the ventricular effective refractory period (VERP) and to induce ventricular arrhythmias (with single and double extrastimuli). If arrhythmias, such as nonsustained ventricular tachycardia (3–10 beats) or sustained ventricular tachycardia (>10 beats), were induced, the protocol was repeated to determine reproducibility. After baseline measurements were completed, isoproterenol (100 μg) was administered intraperitoneally and the protocols were repeated[43,44].

Statistical analysis. Values are presented as means ± s.e.m. Differences between groups were examined for statistical significance using Student's *t*-test or ANOVA. *P* values of < 0.05 were regarded as significant.

Other methods. Other methods are listed in the **Supplementary Methods** online.

GenBank accession number. Mouse *Sema3a*, NM_009152.

Note: Supplementary information is available on the Nature Medicine website.

ACKNOWLEDGMENTS

We are grateful to J. Robbins (Cincinnati Children's Hospital) for the expression vector containing the α-myosin heavy chain promoter. We also thank Y. Tanimoto, Y. Miyake, H. Kawaguchi, E. Kobayashi and M. Nakamura for technical assistance. We are also grateful to the members of the Fukuda laboratory for their comments on the manuscript. This study was supported in part by research grants from the Ministry of Education, Culture, Sports, Science and Technology, Japan, and the Program for Promotion of Fundamental Studies in Health Sciences of the National Institute of Biomedical Innovation.

AUTHOR CONTRIBUTIONS

M.I. designed the study, conducted all experiments, and wrote the manuscript. H.K. and K.K. conducted histochemical characterization. F.H. participated in subcloning. Y.I. conducted the growth cone collapse assay. M.T. provided *Sema3a*$^{-/-}$ mice and *Sema3a*$^{lacZ/lacZ}$ mice. S.M., J.-K.L and I.K participated in and provided advice on the electrophysiology. K.M. and Y.T. participated in histochemical characterization. K.S. conducted the pronuclear microinjection. S.M. and M.S. participated in northern blotting and western blotting. S.O. provided advice on the experimental design. K.F. supported financially and supervised the whole project.

COMPETING INTERESTS STATEMENT

The authors declare no competing financial interests.

Published online at http://www.nature.com/naturemedicine
Reprints and permissions information is available online at http://npg.nature.com/reprintsandpermissions

1. Crick, S.J. *et al.* Innervation of the human cardiac conduction system. A quantitative immunohistochemical and histochemical study. *Circulation* **89**, 1697–1708 (1994).
2. Randall, W.C., Szentivanyi, M., Pace, J.B., Wechsler, J.S. & Kaye, M.P. Patterns of sympathetic nerve projections onto the canine heart. *Circ. Res.* **22**, 315–323 (1968).
3. Ito, M. & Zipes, D.P. Efferent sympathetic and vagal innervation of the canine right ventricle. *Circulation* **90**, 1459–1468 (1994).
4. Crick, S.J., Sheppard, M.N., Ho, S.Y. & Anderson, R.H. Localisation and quantitation of autonomic innervation in the porcine heart I: conduction system. *J. Anat.* **195**, 341–357 (1999).
5. Chow, L.T., Chow, S.S., Anderson, R.H. & Gosling, J.A. Innervation of the human cardiac conduction system at birth. *Br. Heart J.* **69**, 430–435 (1993).

6. Hansson, M., Kjorell, U. & Forsgren, S. Increased immunoexpression of atrial natriuretic peptide in the heart conduction system of the rat after cardiac sympathectomy. *J. Mol. Cell. Cardiol.* **30**, 2047–2057 (1998).
7. Cao, J.M. *et al.* Nerve sprouting and sudden cardiac death. *Circ. Res.* **86**, 816–821 (2000).
8. Cao, J.M. *et al.* Relationship between regional cardiac hyperinnervation and ventricular arrhythmia. *Circulation* **101**, 1960–1969 (2000).
9. Opthof, T. *et al.* Dispersion of refractoriness in canine ventricular myocardium. Effects of sympathetic stimulation. *Circ. Res.* **68**, 1204–1215 (1991).
10. Priori, S.G. & Corr, P.B. Mechanisms underlying early and delayed afterdepolarizations induced by catecholamines. *Am. J. Physiol.* **258**, H1796–H1805 (1990).
11. Ieda, M. *et al.* Endothelin-1 regulates cardiac sympathetic innervation in the rodent heart by controlling nerve growth factor expression. *J. Clin. Invest.* **113**, 876–884 (2004).
12. Kuruvilla, R. *et al.* A neurotrophin signaling cascade coordinates sympathetic neuron development through differential control of TrkA trafficking and retrograde signaling. *Cell* **118**, 243–255 (2004).
13. Puschel, A.W., Adams, R.H. & Betz, H. Murine semaphorin D/collapsin is a member of a diverse gene family and creates domains inhibitory for axonal extension. *Neuron* **14**, 941–948 (1995).
14. Kawasaki, T. *et al.* Requirement of neuropilin 1-mediated Sema3A signals in patterning of the sympathetic nervous system. *Development* **129**, 671–680 (2002).
15. Tanelian, D.L., Barry, M.A., Johnston, S.A., Le, T. & Smith, G.M. Semaphorin III can repulse and inhibit adult sensory afferents *in vivo*. *Nat. Med.* **3**, 1398–1401 (1997).
16. Taniguchi, M. *et al.* Disruption of semaphorin III/D gene causes severe abnormality in peripheral nerve projection. *Neuron* **19**, 519–530 (1997).
17. Behar, O., Golden, J.A., Mashimo, H., Schoen, F.J. & Fishman, M.C. Semaphorin III is needed for normal patterning and growth of nerves, bones and heart. *Nature* **383**, 525–528 (1996).
18. Pashmforoush, M. *et al.* Nkx2-5 pathways and congenital heart disease; loss of ventricular myocyte lineage specification leads to progressive cardiomyopathy and complete heart block. *Cell* **117**, 373–386 (2004).
19. Tago, H., Kimura, H. & Maeda, T. Visualization of detailed acetylcholinesterase fiber and neuron staining in rat brain by a sensitive histochemical procedure. *J. Histochem. Cytochem.* **34**, 1431–1438 (1986).
20. Kupershmidt, S. *et al.* Replacement by homologous recombination of the minK gene with lacZ reveals restriction of minK expression to the mouse cardiac conduction system. *Circ. Res.* **84**, 146–152 (1999).
21. Shusterman, V. *et al.* Strain-specific patterns of autonomic nervous system activity and heart failure susceptibility in mice. *Am. J. Physiol. Heart Circ. Physiol.* **282**, H2076–H2083 (2002).
22. Saba, S., London, B. & Ganz, L. Autonomic blockade unmasks maturational differences in rate-dependent atrioventricular nodal conduction and facilitation in the mouse. *J. Cardiovasc. Electrophysiol.* **14**, 191–195 (2003).
23. Gulick, J., Subramaniam, A., Neumann, J. & Robbins, J. Isolation and characterization of the mouse cardiac myosin heavy chain genes. *J. Biol. Chem.* **266**, 9180–9185 (1991).
24. Kitsukawa, T. *et al.* Neuropilin-semaphorin III/D-mediated chemorepulsive signals play a crucial role in peripheral nerve projection in mice. *Neuron* **19**, 995–1005 (1997).
25. Xu, X.M. *et al.* The transmembrane protein semaphorin 6A repels embryonic sympathetic axons. *J. Neurosci.* **20**, 2638–2648 (2000).
26. Wright, D.E., White, F.A., Gerfen, R.W., Silos-Santiago, I. & Snider, W.D. The guidance molecule semaphorin III is expressed in regions of spinal cord and periphery avoided by growing sensory axons. *J. Comp. Neurol.* **361**, 321–333 (1995).
27. Tang, X.Q., Tanelian, D.L. & Smith, G.M. Semaphorin3A inhibits nerve growth factor-induced sprouting of nociceptive afferents in adult rat spinal cord. *J. Neurosci.* **24**, 819–827 (2004).
28. Dae, M.W. *et al.* Heterogeneous sympathetic innervation in German shepherd dogs with inherited ventricular arrhythmia and sudden cardiac death. *Circulation* **96**, 1337–1342 (1997).
29. Qu, J. & Robinson, R.B. Cardiac ion channel expression and regulation: the role of innervation. *J. Mol. Cell. Cardiol.* **37**, 439–448 (2004).
30. Sosunov, E.A. *et al.* Long-term electrophysiological effects of regional cardiac sympathetic denervation of the neonatal dog. *Cardiovasc. Res.* **51**, 659–669 (2001).
31. Stramba-Badiale, M., Lazzarotti, M. & Schwartz, P.J. Development of cardiac innervation, ventricular fibrillation, and sudden infant death syndrome. *Am. J. Physiol.* **263**, H1514–H1522 (1992).
32. Chantranuwat, C. *et al.* Sudden, unexpected death in cardiac transplant recipients: an autopsy study. *J. Heart Lung Transplant.* **23**, 683–689 (2004).
33. Gitler, A.D., Lu, M.M. & Epstein, J.A. PlexinD1 and semaphorin signaling are required in endothelial cells for cardiovascular development. *Dev. Cell* **7**, 107–116 (2004).
34. Gu, C. *et al.* Neuropilin-1 conveys semaphorin and VEGF signaling during neural and cardiovascular development. *Dev. Cell* **5**, 45–57 (2003).
35. Kuo, H.C. *et al.* A defect in the Kv channel-interacting protein 2 (KChIP2) gene leads to a complete loss of I(to) and confers susceptibility to ventricular tachycardia. *Cell* **107**, 801–813 (2001).
36. Brunet, S. *et al.* Heterogeneous expression of repolarizing, voltage-gated K+ currents in adult mouse ventricles. *J. Physiol. (Lond.)* **559**, 103–120 (2004).
37. Costantini, D.L. *et al.* The homeodomain transcription factor Irx5 establishes the mouse cardiac ventricular repolarization gradient. *Cell* **123**, 347–358 (2005).
38. Takahashi, T. *et al.* Increased cardiac adenylyl cyclase expression is associated with increased survival after myocardial infarction. *Circulation* **114**, 388–396 (2006).
39. Patel, T.D., Jackman, A., Rice, F.L., Kucera, J. & Snider, W.D. Development of sensory neurons in the absence of NGF/TrkA signaling *in vivo*. *Neuron* **25**, 345–357 (2000).
40. Mohler, P.J. *et al.* Ankyrin-B mutation causes type 4 long-QT cardiac arrhythmia and sudden cardiac death. *Nature* **421**, 634–639 (2003).
41. Ecker, P.M. *et al.* Effect of targeted deletions of beta1- and beta2-adrenergic-receptor subtypes on heart rate variability. *Am. J. Physiol. Heart Circ. Physiol.* **290**, H192–H199 (2006).
42. Heart rate variability: standards of measurement, physiological interpretation and clinical use. Task Force of the European Society of Cardiology and the North American Society of Pacing and Electrophysiology *Circulation* **93** 1043 1065 (1996).
43. Wehrens, X.H. *et al.* Protection from cardiac arrhythmia through ryanodine receptor-stabilizing protein calstabin2. *Science* **304**, 292–296 (2004).
44. Kannankeril, P.J. *et al.* Mice with the R176Q cardiac ryanodine receptor mutation exhibit catecholamine-induced ventricular tachycardia and cardiomyopathy. *Proc. Natl. Acad. Sci. USA* **103**, 12179–12184 (2006).